Evaluation of Machine Learning Algorithms for the Classification of Lake Ice and Open Water from Sentinel-3 SAR Altimetry Waveforms

by

Jaya Sree Mugunthan

A thesis

presented to the University of Waterloo

in fulfillment of the

thesis requirement for the degree of

Master of Science

in

Geography

Waterloo, Ontario, Canada, 2023

Author's Declaration

I hereby declare that I am the sole author of this thesis. This is a true copy of the thesis, including any required final revisions, as accepted by my examiners.

I understand that my thesis may be made electronically available to the public.

Abstract

Lakes cover a significant fraction of the landscape in many northern countries. They play a key role in regulating weather and climate and also have a significant impact on northern communities since the presence (or absence), extent and thickness of lake ice affect transportation (ice roads), food availability, recreational activities, and tourism in wintertime. The drastic decline in in-situ observations of lake ice phenology (i.e., freeze-up and break-up dates and ice cover duration) and lake ice thickness globally over the last three decades make remote sensing technology a viable means for monitoring lake ice conditions. Although satellite radar altimetry has been used in various cryospheric and hydrological studies, little work has been conducted on lake ice compared to, for example, sea ice and the estimation of lake water levels.

This study was carried out using Sentinel-3A/B SAR altimetry data acquired over three ice seasons (2018-2019, 2019-2020 and 2020-2021) at 11 large lakes across the Northern Hemisphere. We explored the information provided by radar waveforms to discriminate between open water, first (young) ice, growing ice and melting ice using machine learning models. To characterize the waveforms, seven waveform parameters were derived: Leading Edge Width (LEW), Offset Center of Gravity (OCOG) Width, Pulse Peakiness (PP), backscatter coefficient (Sigma0), late tail to peak power (LTTP), early tail to peak power (ETTP) and the maximum value of the echo power. Four machine learning algorithms including Random Forest (RF), Gradient Boosting Trees (GBT), K Nearest Neighbour (KNN) and Support Vector Machine (SVM) classifiers were tested to assess their capability in classifying the lake surfaces across all years. Manual class labelling based on Sentinel-3 Synthetic Aperture Radar Altimeter (SRAL) waveforms and complementary satellite data (Sentinel-1 imaging SAR data, Sentinel-2 Multispectral Instrument (MSI) Level 1C data, and MODIS Aqua/Terra data) was performed to create training and test samples for the classifiers. Accuracies greater than 95% were achieved across all classifiers using a 4-parameter combination (Sigma0, PP, OCOG Width, and LEW). Amongst all waveform parameters, Sigma0, OCOG width and PP were found to be the most important parameters for discriminating between lake ice and open water. Despite showing comparable classification performances in the overall classification, RF and KNN are found to be a better fit for global lake ice mapping as both are less sensitive to their internal hyperparameters and have faster processing speeds. Additionally, consistent results

(>93.7% accuracy in all classifiers) achieved on the accuracy assessment carried out for each lake revealed the strength of the classifiers for spatial transferability. Implementation of RF and KNN could be valuable in a pre-or post-processing step for identifying lake surface conditions under which the retrieval of water level and ice thickness may be limited or not possible and, therefore, inform algorithms currently used for the generation of operational or research products. While the research focused on 11 of the largest lakes of the Northern Hemisphere, the classification approach has potential for application on smaller lakes too since SAR mode data (~300 m along-track resolution) is used in the study.

Keywords: SAR altimetry, lake ice, classification, waveform, machine learning

Acknowledgements

First and foremost, I would like to express my deepest gratitude to my supervisor, Dr. Claude Duguay for his continuous support, patience, encouragement, and expert guidance over the years (from summer internship to Master's). I would also like to thank him for believing in me and providing me with numerous opportunities.

I would also like to add my sincere thanks to my thesis committee members Dr. Richard Kelly and Dr. Grant Gunn.

I would also like to thank Dr. Elena Zakharova for providing guidance and for clarifying all my doubts about altimetry.

A special thanks to Claude's research group members for their warm and continued support. I also want to thank my friend Marzieh Foroutan for her friendly support and encouragement when I first came to Canada as an intern. I wish you were here with me to share this happy moment.

Last but not least, I am grateful to my mom Sethirabalammal and my brother Sri Hari for their unwavering support and encouragement throughout my life. I would also like to extend thanks to all my friends for their continued support.

Table of Contents

List of Figures

List of Tables

Chapter 1

General Introduction

1.1 Motivation

Lakes are effective sentinels for climate change since their physical, chemical, and biological properties respond quickly to changes associated with climate (Rosenzweig et al., 2007; Adrian et al., 2009). As the response variables are major determinants of the changes in the lake properties and can act as indicators of climate change, the Global Climate Observing System (GCOS) recognizes lakes as an Essential Climate Variable (ECV) and in particular the following six thematic products - lake surface water temperature, lake water extent, lake water level, lake ice cover, lake ice thickness and lake colour (lake water-leaving reflectance) (Belward et al., 2016; Buontempo et al., 2022). Changes in lake surface water temperature and water level have been documented globally (Birkett et al., 2011; Crétaux et al., 2011; Sharma et al., 2015; Carrea & Merchant, 2019). In the Northern Hemisphere, changes in lake ice cover/phenology, and to a lesser extent ice thickness, have also been documented largely from in situ observations (e.g., Sleator, 1995; NSIDC, 1995; Benson et al., 2000; NSIDC, 2004; Sharma et al., 2021). Historical satellite records are increasing in length, especially since the 1990s, and there has also been significant progress made in the development of retrieval algorithms (e.g., Du et al., 2017; Wu et al., 2021; Cai et al., 2022), such that satellite remote sensing is playing an increasingly important role in monitoring lakes globally (Duguay et al., 2015).

One of the satellite technologies used for monitoring changing lake conditions is radar altimetry. Unlike imaging sensors, altimetry instruments are profiling systems that collect information in the form of radar echoes along the earth surface (i.e., tracks). Such radar echoes are recorded as a histogram of energy backscattered by the ground surface to the satellite with respect to time; they are referred to as waveforms. Radar altimetry has been widely used in the monitoring of lake water levels in the past few decades (Birkett, 1995; Crétaux & Birkett, 2006; Sarmiento & Khan, 2010; Shu et al., 2020a; Ziyad et al., 2020) and serves as an essential contributor for many globally distributed water level databases such as Hydroweb, G-REALM, DAHITI and the European Space Agency's (ESA) CCI Lake product (Crétaux et al., 2011; Birkett et al., 2011; Schwatke et al., 2015; Crétaux et al., 2020). Compared to, for example, sea ice and the estimation

of ocean and lake water levels, little attention has been given to the application of radar altimetry data to monitor lake ice cover or estimate lake ice thickness. Although altimetry has been used to estimate water level in lakes, it has only recently been recognized that the presence of ice cover and its growth during the winter season introduces errors in the retrieval of water level estimates (Birkett & Beckley, 2010; Sarmiento & Khan, 2010; Ricko et al., 2012; Shu et al., 2020a; Nielsen et al., 2020). This water level retrieval error happens as the presence of ice modifies the shape of the radar echoes, which in turn, affects height estimations (Tseng et al., 2013). To resolve this limitation, it would be helpful to know the surface types of the lake surface so that one could avoid such bias-inducing observations or estimate any other equivalent measurements. Even in the context of lake ice thickness estimation, knowledge of the surface types associated with each altimetry observation is useful. This is because the current altimetry-based lake ice thickness (LIT) retrieval algorithms fail to provide true thickness estimates until the young ice reaches a certain thickness or as soon as melt onset begins (Mangilli et al., 2022).

To date, algorithms to determine the presence of ice and open water from altimetric missions have relied on the combination of brightness temperature and backscatter (low-resolution mode or LRM) measurements (Kouraev et al., 2003; Kouraev et al., 2007). Using simultaneous multi-frequency radiometer (18 to 37 GHz) and radar altimetry data (Ku-band) from several satellites (TOPEX/Poseidon, Jason-1, ENVISAT, Geosat Follow-On), Kouraev et al., 2007 conducted a case study on Lake Baikal and demonstrated the potential of satellite altimetry and radiometry to discriminate between lake ice and open water. Linear equations developed from simple classification thresholds paved the way to determine freeze-up and break-up dates on large lakes in relation to atmospheric forcings (Kouraev et al., 2008). Ziyad et al. (2020) proposed a threshold-based method to classify ice-covered and open water areas in Canadian lakes (Great Slave Lake, Lake Athabasca, Lake Winnipeg, and Lake of the Woods) during freeze and thaw periods. The authors used three different parameters extracted from the Jason-2 radar (Ku-band) altimetry data, including backscatter coefficient, brightness temperature (average value of the brightness temperature at 18.7 GHz and 37 GHz) and pulse peakiness to create the threshold-based algorithm. Using simultaneous brightness temperature measurements provided by microwave radiometer channels at 23.8 GHz and 36.5 GHz onboard the Sentinel-3 satellite mission, Shu et al. (2020a) were able to detect the presence of ice in several lakes. Both Ziyad et al. (2020) and Shu et al. (2020a) developed classification approaches with in mind the presence of ice as a limiting

factor in the estimation of lakes water levels (i.e., the presence of ice in lakes introduces biases in water level estimates).

The magnitude and the shape of a radar echo (waveform) vary with the properties/conditions of the target surface. Thus, one approach for discriminating between ice cover and open water is to extract waveform parameters that define the waveform. This approach has most notably been applied to sea ice (Zygmuntowska et al., 2013; Ricker et al., 2014; Nilsson et al., 2015; Wernecke & Kaleschke, 2015; Rinne & Similä, 2016; Shen et al., 2017; Shen et al., 2017; Müller et al., 2017; Shu et al., 2020b; Fredensborg Hansen et al., 2021) and in a more limited extent to lake ice (Ziyad et al., 2020). Given the limited research on the topic of lake ice from radar altimetry and in light of recent and upcoming altimeter missions offering data in higher-resolution synthetic aperture radar (SAR) mode (e.g., Sentinel-3, Sentinel-6, Surface Water and Ocean Topography (SWOT)), this thesis focuses on assessing machine learning (ML) algorithms applied to SAR altimetry data from the Sentinel-3 mission to classify ice and open water over a selection of large lakes across the Northern Hemisphere.

1.2 Research objectives

The main goal of this research is to evaluate the capability of different machine learning algorithms in discriminating between open water and lake ice using waveform parameters and backscatter coefficients. To achieve this goal, the following objectives are set:

1) Determine the optimal parameter combination to achieve the best classification performance and calculate the feature importance.

2) Examine the sensitivity of the classifiers to their internal hyperparameters and find the best hyperparameters for the study.

3) Evaluate the capability of the classifiers to cope with spatial heterogeneity in the dataset.

1.3 Thesis Outline

Including this introduction chapter, this thesis is organized into four chapters. Chapter 2 reviews the existing literature to provide background on lake ice, satellite altimetry and waveform parameter-based classification. Chapter 3 contains the draft of a paper to be submitted to the journal *Remote Sensing of Environment*, titled "Machine Learning Based Classification of Lake ice and Open Water from SAR Altimetry Waveform Parameters". Finally, Chapter 4 summarizes the study, identifies some limitations, and provides recommendations for future work.

Chapter 2

Background

2.1. Lake Ice Phenology

The term 'lake ice phenology' defines the stages of lake ice formation, ice-covered duration and ice decay (Duguay et al., 2015). In other words, lake ice phenology comprises three main periods: 1) freeze-up, 2) ice growth, and 3) break-up. These periods occur as a result of an energy surplus or deficit in the energy balance of the lake ice cover (Carrea et al., 2015).

2.1.1 Freeze-up

Freeze-up refers to the duration between the start of ice formation and the establishment of a complete sheet of ice on a lake surface (Kang et al., 2012). Freeze-up occurs during the fall/ early winter. Timing varies depending on the morphometry and latitude of the lake, and weather/climate conditions (Brown & Duguay, 2010). Once the temperature of the lake falls to 4° C (the temperature at which freshwater reaches its maximum density), due to heat loss, the surface water becomes denser and sinks. This process repeats itself until all the water column reaches its maximum density. With further cooling and ceased of mechanical mixing, a thin layer of ice forms on the surface when the surface water cools to the freezing point. This initial layer of ice is called skim ice, which often forms first at the calm, protected borders of the lake. This ice development process can happen several times until the lake surface becomes entirely ice-covered (Jeffries et al., 2005).

Over the ice season, two types of ice may be observed in lakes: 1) congelation ice (Figure 2-1 (a)) and 2) snow ice (Figure 2-1 (b)). Ice that usually forms first and is comparatively clear is called congelation ice (Brown & Duguay, 2010). It is also referred to as "black ice" as the underlying water is clearly visible. This dark appearance occurs due to its high optical depth/significant light transmittance (Jeffries et al., 2005). Water freezing at the base of the initial ice layer results in the thickening of the skim ice and the formation of congelation ice growing downward. Such basal freezing and ice formation produce two distinct texture types of ice. One is the most common and has horizontally oriented c-axes (S1) with a columnar texture of vertically

elongated crystals. The other has vertical c-axes (S2) of many massive crystals. Comparatively, S1 ice has a higher albedo than S2 ice (Jeffries et al., 2005).

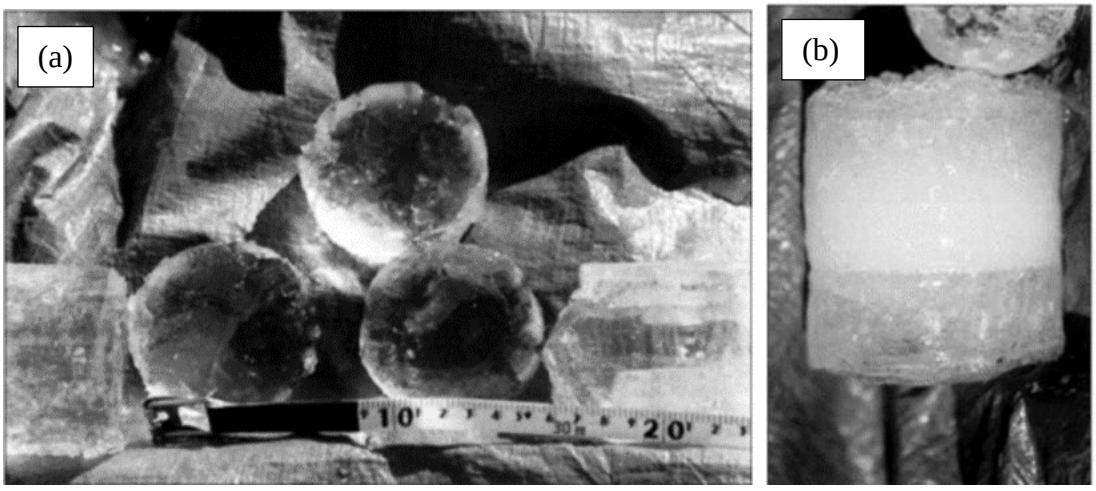

Figure 2- 1 (a) Congelation ice and (b) Snow ice (Source: Duguay et al. 2002)

The second dominant lake ice type, particularly prevalent at mid-latitude lake locations, is snow ice which is often referred to as "white ice" due to its high light scattering and albedo (Jeffries et al., 2005). White ice can be formed in two ways. One is when the snow mass on the ice surface is large enough to overcome the buoyancy of the ice and pushes the ice surface below the piezometric water level. Thus, flooding at the snow-ice interface occurs and leads to slush formation. Rapid freezing of the slush forms snow-ice (Ashton, 2011). The other way of snow ice formation happens when the meltwater or rainwater seeps through the snow to the ice layer and eventually becomes frozen (Bengtsson, 1986).

2.1.2 Ice growth

Temperature and precipitation are the leading factors that influence lake ice during its growth season (Brown & Duguay, 2010). Adams (1976) found that ice growth occurs as the heat continues to be released from the lake through the upper ice surface. This heat loss happens due to the temperature gradient difference between the underlying warmer water and the colder air above. Trends in ice thickness have also been linked to variations in air temperature. In addition, snow on ice influences ice growth. A larger amount of snowfall over lake ice leads to snow ice formation, which enhances ice growth and influences the composition of lake ice (Brown and Duguay, 2010).

2.1.3 Break-up

The breakup process majorly comprises decay and fracture; however, in some scenarios, ice drifting may happen on large lakes and later gets removed by outflowing rivers (Jeffries et al., 2012). The ice disintegration process is regulated by several factors, including heat input from the atmosphere, state of ice and snow, wind, fluxes, and inflow from streams/ land runoff (Brown & Duguay, 2010; Williams, 1965). Break up usually happens sequentially, at first, snow, then snow ice (if any) and finally, black ice melts. However, the rapid break-up may take place in the presence of clear ice as it absorbs more shortwave radiation due to its low albedo nature (Kang et al., 2012). Due to the changes happening both at the ice surface and internally, the albedo varies over the season. The albedo of the lake ice reduces with the porosity of the ice cover and increases with the minimum ice density (Heron & Woo, 1994). Heron & Woo (1994) also observed that the thawing of overlying c-axis ice crystals (vertical orientation) causes an albedo decrease from 0.45 to 0.2. This albedo decline exposes the underlying c-axis ice (horizontal orientation) crystals where the inner melting has not started yet.

2.2 Satellite radar altimetry

2.2.1 Satellite altimeter missions

The first altimeter satellite, Skylab, was launched in 1973. It was the first experimental mission sent out to space with the primary goal of determining the geoid based on the concept of altimetry. With further improvements in the altimeter system, GEOS-3 was launched in 1975. Successively, SEASAT and GEOSAT were launched in 1978 and 1985. These missions were beneficial in further understanding the altimetry technique, thereby helping to improve the range precision and accuracy of the orbit in future missions (PODAAC, 2022). However, these satellites were short-lived, and the altimeter era was considered to begin only in 1991 with the launch of the ERS-1 satellite by the European Space Agency (ESA). Following ERS-1, several altimeter satellite missions (Table 2-1) were launched into space and started providing continuous altimetric measurements. Figure 2-2 shows the past, present and future radar altimetry missions.

Table 2- 1 Satellite altimetry missions and their main characteristics (Aviso+, 2022)

Mission	Operational time	Altitude (Km)	Inclination (°)	Revisit time	Bands
ERS-1	1991-2000	785	98.52	35	Ku
Topex/Poseidon	1992-2006	1336	66	10	Ku, C/Ku
ERS-2	1995-2011	785	98.52	35	Ku
GFO	1998-2008	800	108	17	Ku
Jason-1	2001-2013	1336	66	10	Ku, C
Envisat	2002-2012	800	98.55	35	Ku, S
Jason-2	2008-2019	1336	66	10	Ku, C
Cryosat-2	2010-present	717	92	369	Ku
HY-2A	2011-2020	971	99.3	14	Ku, C
SARAL	2013-present	800	98.55	35	Ka
Jason-3	2016-present	1336	66	10	Ku, C
Sentinel-3A	2016-present	815	98.6	27	Ku, C
Sentinel-3B	2018-present	815	98.6	27	Ku, C
CFOSAT	2018-present	500	97	13	Ku
HY-2B	2018-present	973	99.3	14	Ku, C
HY-2C	2020-present	958	66	10	Ku, C
Sentinel-6 MF/ Jason-CS	2020-present	1336	66	10	Ku, C
HY-2D	2021-present	971	66	10	Ku, C

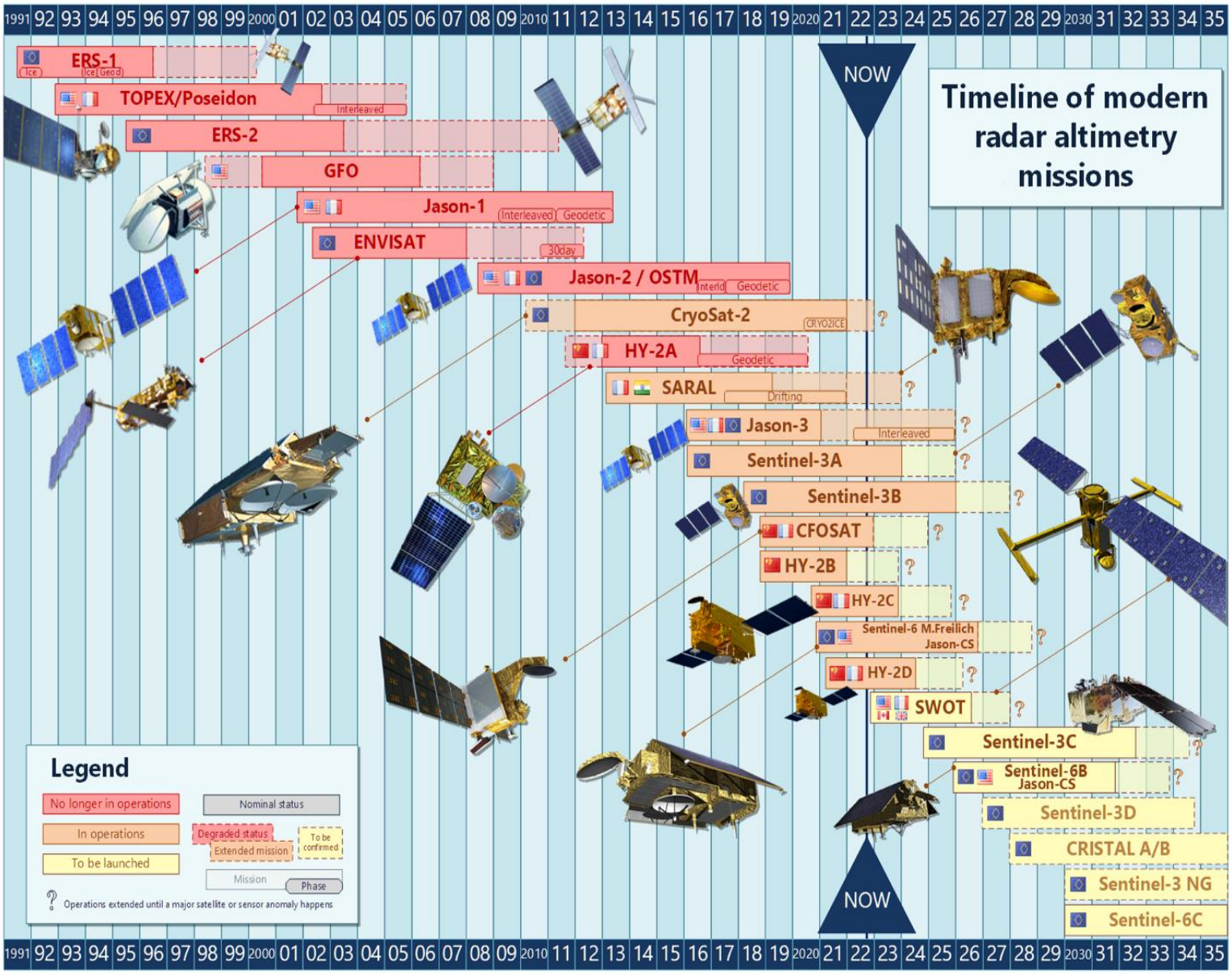

Figure 2- 2 Timeline of the radar altimetry missions since 1991. Source: Aviso+ (2022)

2.2.2 Basic principle of satellite radar altimetry

In satellite radar altimetry, a nadir-pointing satellite carrying an altimeter system sends a series of microwave pulses to the target on the Earth. These pulses get reflected by the target to the satellite and are recorded in the form of echoes. The two-way travel time between the transmission and reception of the radar pulse is used to measure the surface height (distance

between the satellite and the surface of the target) through the range measurement. Figure 2-3 presents the basic principle of satellite altimetry. The range $\hat{R}$ is calculated (Fu and Cazenave, 2000) as

$$\hat{R} = \frac{ct}{2} \tag{2.1}$$

where c is the speed of light in vacuum (~3x10^8 ms^{-1}), and *t* is the time the signal takes to travel from the satellite to the target and its way back to the satellite. As the signal travels through the atmosphere, it gets affected by the refraction from the particles. This interaction with particles reduces the speed of the signal. Hence, the range $\hat{R}$ needs to be corrected for various components (ΔR_j) of atmospheric refraction, instrumental bias and sea-state effects (Fu and Cazenave, 2000). The corrected range R is estimated by

$$R = \hat{R} - \sum_j \Delta R_j \tag{2.2}$$

Using the corrected range measurement, the surface height *h* can be easily calculated by

$$h = H - R \tag{2.3}$$

where H is the height (altitude) of the satellite relative to the reference ellipsoid and can be obtained by the orbital parameters of the satellite.

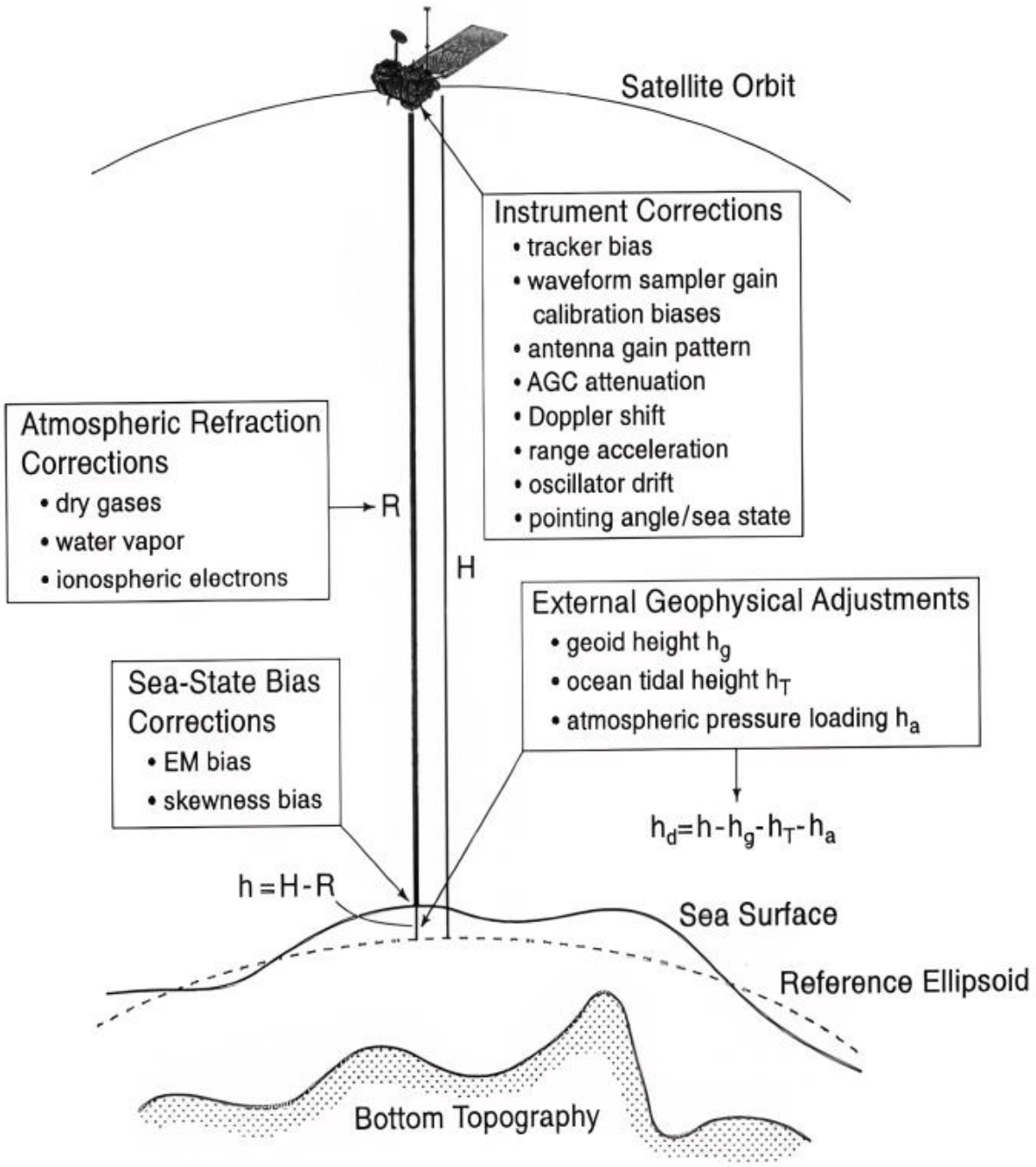

Figure 2- 3 A schematic of the principle of satellite altimetry (Source: Fu and Cazenave, 2000)

2.2.3 Conventional and delay/Doppler altimeters

The signal reflected from the target is sampled as the reflected power over time, referred to as waveform or radar echo. In other words, a waveform represents a histogram of energy backscattered by the target surface with respect to time. Interestingly, the construction of the waveform and the area illuminated on the target surface differs with the type of altimeter system used aboard the satellite. Currently, two types of altimeter systems are widely in use: conventional and delay/Doppler altimeters. Figure 2-4 presents the comparison of the above-mentioned altimeters and the waveforms constructed by them. Conventional altimeters are often referred to as Low-Resolution Mode (LRM) or pulse-limited altimeters. This is because the area illuminated by the LRM altimeters is limited by the width of the transmitted pulse from the altimeter systems. In contrast, the area illuminated by the delay/Doppler altimeters called Synthetic Aperture Radar Mode (SARM) altimeters depends on the beamwidth of the radar used in the altimeter instrument. Hence, SARM altimeters are called beam-limited altimeters.

Although there is a long history of pulse-limited satellites, SARM altimeters are considered more advantageous than the pulse-limited ones as they efficiently utilize the power reflected from the surface using the delay/Doppler technique. Through the SAR processing mode, groups of transmitted pulses collected along the satellite track are coherently processed and thus offer multi-look processing, resulting in a high-resolution dataset (Raney, 1998). Figure 2-5 illustrates the sampling of a LRM and a SAR waveform at 1Hz and 20 Hz.

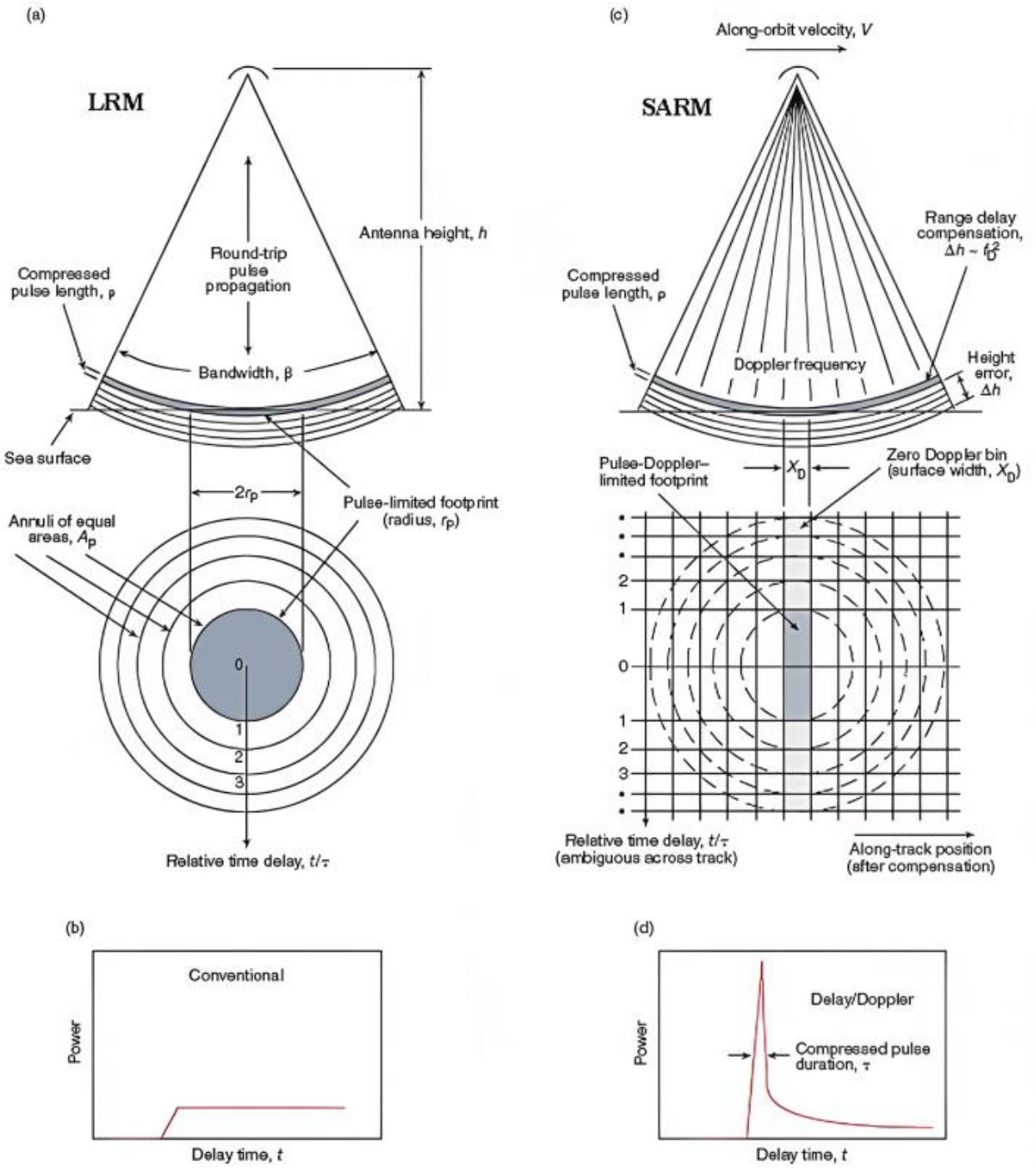

Figure 2- 4 Comparison of conventional altimeter's (a) illumination geometry (side view) and footprint (plan view) and (b) LRM waveform to a delay/Doppler altimeter's (c) illumination geometry and footprint and (d) SARM waveform (Source: Raney, 1998; Tournadre & Chaprono, 2020)

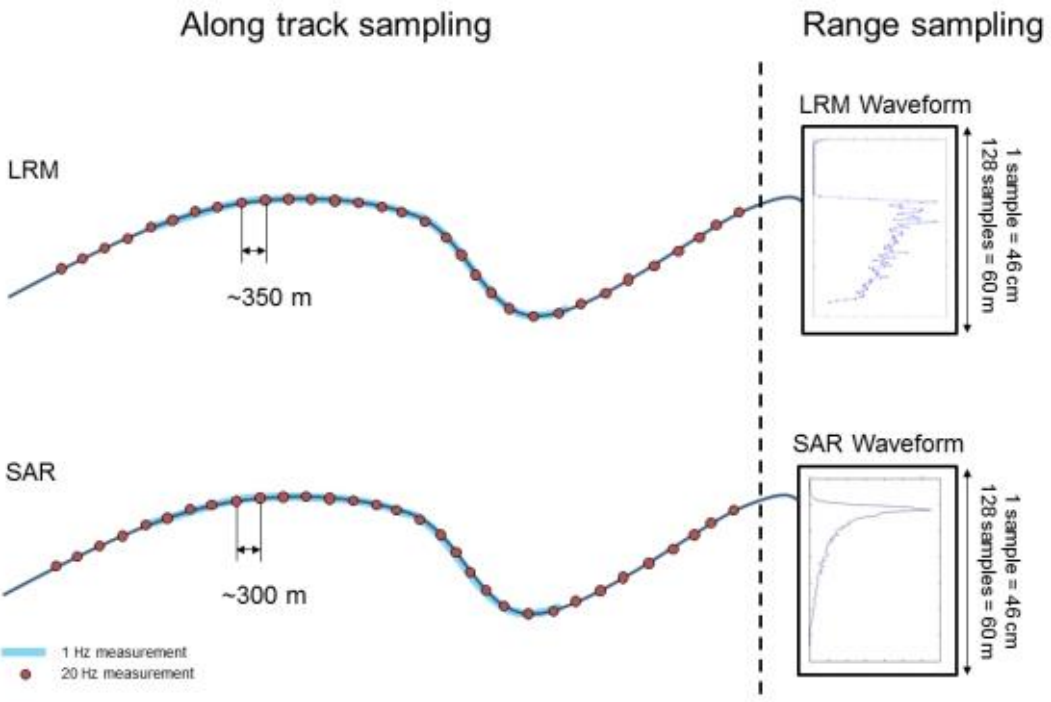

Figure 2- 5 Along track and range sampling of LRM and SAR mode altimeters (Sentinel-3 User Guides, 2022)

2.3 Classification of ice and open water with data from satellite altimetry missions

This section is divided into two subsections to present the background knowledge relevant to the classification approach developed in the study. Section 2.3.1 covers previous studies on the classification of lake ice and open water. An extensive discussion on sea ice studies for surface-type classification methods, including the waveform parameterization approach and ML algorithms, is presented in section 2.3.2.

2.3.1 Lake ice

A combination of active and passive microwave observations from several LRM radar altimetry (Ku-band) missions (TOPEX/Poseidon, Jason-1, ENVISAT and Geosat Follow-On) complemented by SSM/I (Special Sensor Microwave/Imager) passive microwave data were used to develop a threshold-based classification algorithm for discriminating between lake ice and open

water in Lake Baikal (Kouraev et al., 2007). In radar altimetry data, backscatter from young or newly formed ice is high; however, the brightness temperature value is relatively low. Further growth in ice induces a decrease in backscatter values while brightness temperature values gradually increase. Additionally, snow accumulation and ice decay also impact the backscatter and brightness temperature values (Kouraev et al., 2007). According to the authors, backscatter and brightness temperature values are low for open water and high for ice cover, respectively. Since the backscatter and brightness temperature (average of the brightness temperature values at two frequencies) values vary with the formation, growth and decay of the lake ice, Kouraev et al. (2007) applied a threshold limit to these values to distinguish between lake ice and open water. These threshold values are unique to each satellite. Figure 2-6 shows histograms of two distinctive clusters (open water and lake ice) separated by a dashed line (threshold limit) for all altimetry mission data. Threshold values that classify open water and ice are converted into a linear equation and applied to each satellite data. This approach was used to estimate the specific dates for ice formation, the first appearance of open water and the ice-free date.

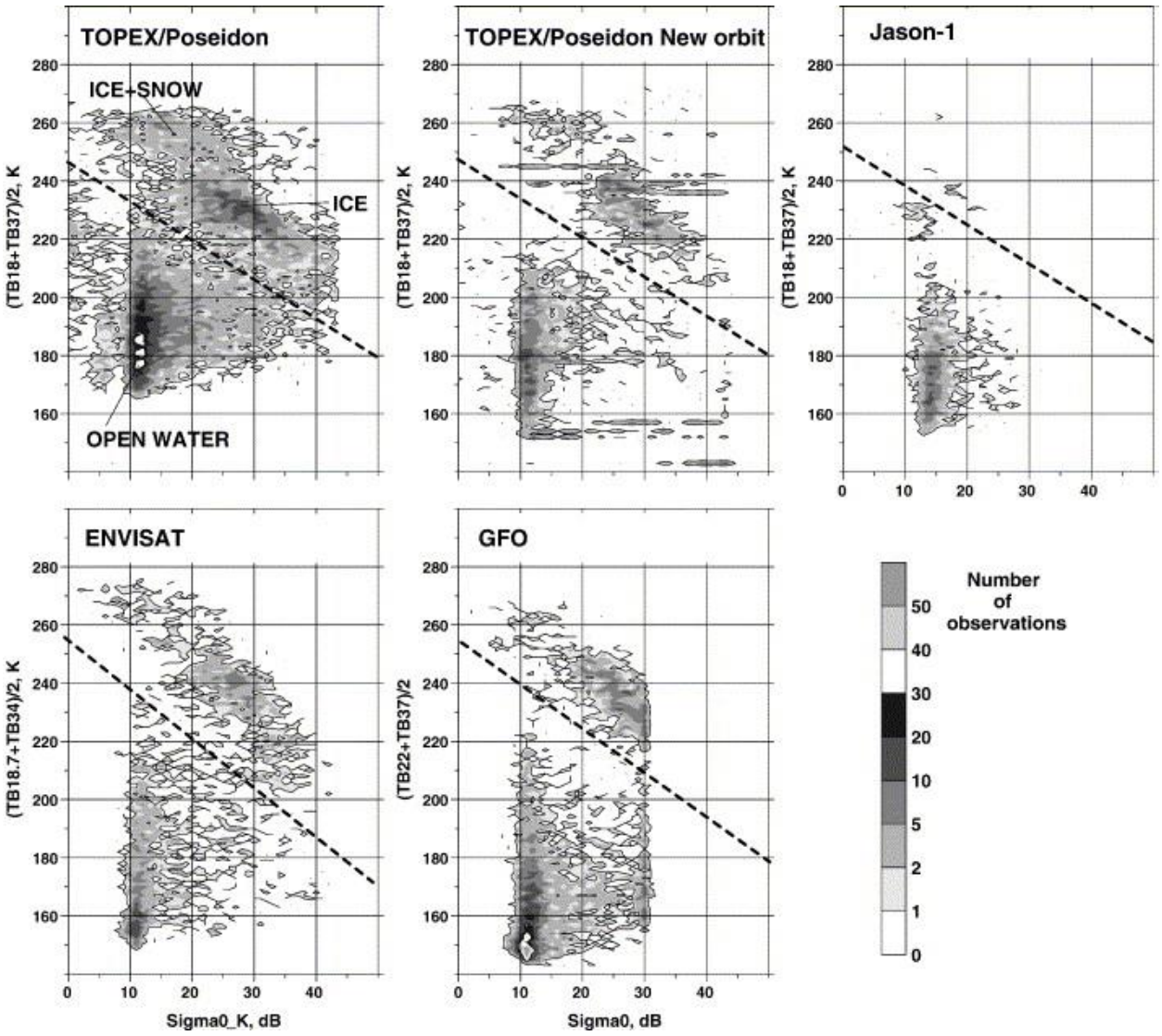

Figure 2- 6 Two-dimensional histograms of several altimetry missions for Lake Baikal (1992-2002). Here the x-axes and y-axes show the backscatter coefficient in Ku-band and the average value of brightness temperature (TB) values at two frequencies. The dashed line represents the separation between open water and lake ice clusters. (Source: Kouraev et al., 2007).

Another classification algorithm proposed by Ziyad et al. (2020) uses pulse peakiness (PP) (derived from LRM radar altimetry waveforms), backscatter coefficient (Ku-band) and brightness temperature values (average value from 18.7 GHz and 37 GHz measurements) of the Jason-2

mission to discriminate between open water and different ice types in Canadian lakes (Great Slave Lake, Lake Athabasca, Lake of the Woods, and Lake Winnipeg). To classify the altimetry observations into different clusters (open water, ice cover, ice freeze-up, and ice break-up), the authors identified the optimal thresholds of the three parameters by implementing unsupervised clustering methods, including K-means and hierarchical clustering. In the study, the backscatter and PP values fluctuated during ice break-up and decreased until they attained stableness during the open water period. During freeze-up, ice cover formation resulted in an increase in these two parameters; however, the parameter values decreased gradually with ice growth. In contrast, brightness temperature values were higher during the ice-covered period and lowered during the open-water season. The temporal variability of backscatter and average brightness temperature values in Ziyad et al. (2020) was nearly similar to that reported in Kouraev et al. (2007). Figure 2-7 presents the annual time series of the monthly averages (red) and standard deviations (black) of the mean value of the parameters, including backscatter, PP and average brightness temperature. These values were obtained along the ascending and descending Jason-2 tracks covering the Great Slave Lake (2008-2016).

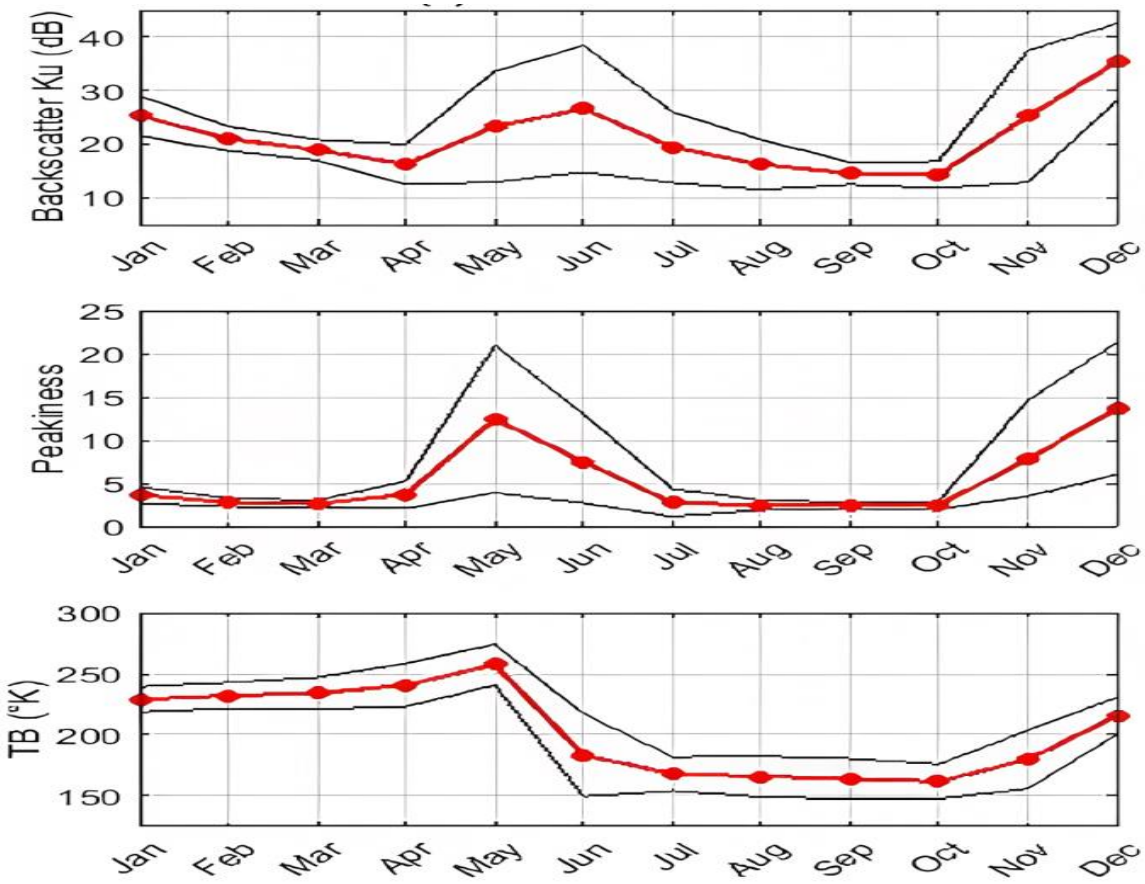

Figure 2- 7 Jason -2 temporal variation of backscatter, peakiness and average brightness temperature values on Great Slave Lake from 8 September 2008 to 21 September 2016. The red and black lines indicate the monthly averages and standard deviations, respectively. computed from the mean value of the parameters (Source: Ziyad et al., 2020)

Since brightness temperature values are sensitive to the ice cover formation (Kang et al., 2012), Shu et al. (2020a) used simultaneous brightness temperature measurements (at 23.8 GHz and 36.5 GHz) provided by the passive microwave radiometer aboard the Sentinel-3 satellite to discriminate between open water and ice. Shu et al. (2020a) conducted a research study on 15 lakes and reservoirs in Finland, Canada, USA, and Sweden to detect the presence of ice using brightness temperature values. Notably, Shu et al. (2020a) did not use altimetry data to classify open water and lake ice. The classification approach was developed as a part of the study, as the main aim was to develop a bimodal correction algorithm to generate temporally consistent lake water levels. As water level estimation depends on altimetry data, the authors analyzed the altimetry waveforms observed throughout the year. Figure 2-8 shows the waveforms observed at Great Slave Lake

during winter 2016-2017. It is important to note that the altimetry waveform shape is unique to each surface type and changes temporally over the ice season. For example, thin ice has a single peak waveform, while growing ice (thick ice) has a waveform with two peaks. Both Ziyad et al. (2020) and Shu et al. (2020a) developed lake ice and open water classification approaches to improve the estimation of lake water levels from altimetry data, as the presence of ice on a lake introduces bias in water level estimates.

Although these previous studies suggested some classification approaches to discriminate between lake ice and open water, the use of radiometry data (brightness temperature measurements) and LRM altimetry data in the classification approaches present some limitations. The former limits the application of the method to very large lakes as the microwave radiometer observes with a large footprint (~10-35 km) and produces coarser-resolution data. The latter leads to a significant data loss as LRM altimetry observations can greatly be affected by land contamination. In addition, LRM data have lower along track & across-track resolution (~2-20 km), which limits the applicability of the method to smaller lakes. The approach developed in this thesis presents an advancement over these previous studies since it focuses on the application of machine learning algorithms applied to high-resolution SARM data (backscatter and waveforms) and without the need of coarse resolution brightness temperature measurements.

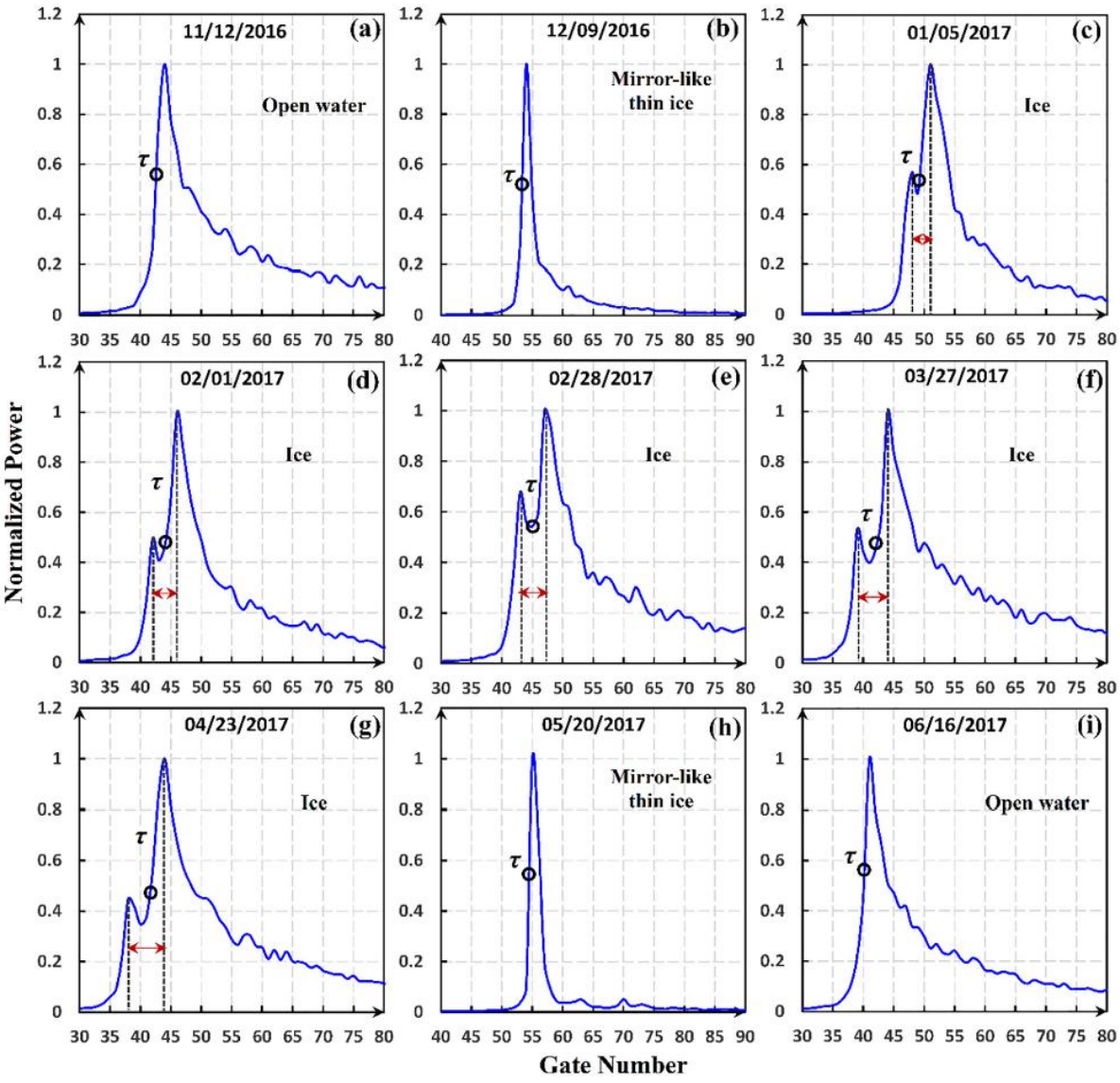

Figure 2- 8 The time series of Sentinel-3 SAR altimetry waveforms observed on Great Slave Lake during the 2016-2017 ice season. The date format is MM/DD/YYYY and τ represents the epochs produced by SAMOSA-3 retracker (Source: Shu et al., 2020a).

2.3.2 Sea ice

Altimetry waveform parameter-based ice cover classification approach has already been proven to have the potential to discriminate between ice and open water and is widely used in many sea ice classification studies. For instance, Zygmuntowska et al. (2013) presented a Bayesian

classification approach based on the maximum power of the waveform (Max), PP, Leading Edge Width (LEW), Trailing Edge Width (TEW) and Trailing Edge Slope (TES) parameters to classify first-year ice (FYI), multi-year ice (MYI) and leads over Arctic Sea ice. Through this method, they were able to classify 80% of the waveforms correctly, and the altimetry data used in the study was obtained from an Airborne Synthetic Aperture and Interferometric Radar Altimeter System operating at Ku- band.

To discriminate between the ocean, lead, and sea ice over Arctic Sea ice, Ricker et al. (2014) developed a threshold-based algorithm using Cryosat-2 (Ku-band) waveform parameters, including PP, stack kurtosis (K), stack standard deviation (SSD), pulse peakiness left (PP_l), pulse peakiness right (PP_r), sea-ice concentration (IC) and the width of the OCOG box (OCOG Width). Wernecke & Kaleschke (2015) also carried out a study over Arctic Sea ice and used several waveform parameters (Max, PP, PP_l, PP_r, LEW, TEW, SSD, K) from Cryosat-2 (Ku-band) data to find an optimized threshold for lead detection. Among all the waveform parameters, a threshold of 2.58 x 10^{-11} Watts on the maximum power of the waveform (Max) performed well (68% accuracy) in discriminating the leads from the sea ice. In addition, a K- Nearest Neighbors (KNN) based classification method was employed by Rinne & Similä (2016) to distinguish different sea ice types (thin FYI, thick FYI and MYI) and open ocean over Arctic Mediterranean (Barents and Kara seas). Cryosat-2 waveform parameters used in the classification approach were PP, LEW, late tail to peak power (LTPP), early tail to peak power (ETPP), SSD, PP_l and PP_r. The automation approach was able to produce an overall classification accuracy of >90% for discriminating between open ocean and ice.

Shen et al. (2017a) applied a random forest (RF) classification based on PP, LEW, TEW, SSD, Max and Sigma0 to distinguish open water, FYI and MYI and achieved an overall accuracy of 85%. In the study, the Cryosat-2 (Ku-band) data acquired over the Arctic Sea ice region was used. Shen et al. (2017b) used the same Cryosat-2 waveform parameters to discriminate between FYI, MYI and open water over Arctic Sea ice by applying six different classifiers, including convolutional neural network (CNN), Bayesian, KNN, Support Vector Machine (SVM), RF, and back propagation neural network (BPNN). In the study, RF scored the highest mean accuracy of 89.15%, followed by Bayesian, SVM, and BPNN classifiers achieving ~86%. Overall, CNN and KNN yielded the lowest classification accuracy of ~82%.

Müller et al. (2017) developed an approach to classify open ocean, sea ice and leads over the Greenland Sea and the Fram Strait by implementing a combination of partitional clustering (K-medoids) and classification method (KNN) based on waveform maximum, trailing edge decline, waveform noise, waveform width, leading edge slope and TES. The authors conducted a quantitative assessment to test the classification performance and achieved an accuracy of 70.7% and 76.9% for Envisat (Ku-band) and SARAL/AltiKa (Ka-band), respectively. Shu et al. (2020b) proposed an Object-based Random Forest (ORF) method to distinguish FYI and MYI over Arctic Sea ice using Cryosat-2 data. The ORF approach used waveform parameters including LEW, TEW, Sigma0, PP, SSD and Max to generate different feature layers and achieved an overall accuracy of 90.1%. Likewise, Fredensborg Hansen et al. (2021) implemented four classifiers, including threshold-based classification, Bayesian classification, KNN and RF based on five SARAL/AltiKa (Ka-band) waveform parameters (Max, PP, LEW, TES and Sigma0) to discriminate between FYI and MYI in the Arctic. For FYI, the authors achieved a high classification performance with an accuracy of 93% (Bayesian classifier); however, for MYI, only 39% classification accuracy (threshold-based classifier) was attained.

The above studies illustrate the possibility of sea ice (FYI/MYI) and open water classification from machine learning approaches, including leads, based on altimeter waveforms and demonstrate that different ice types tend to display distinct waveform shapes. It is also clear that altimetry waveform parameters are useful for discriminating open water and different sea ice types. Thus, this thesis draws the concept of parameterization from the above-mentioned literature to implement and assess machine learning algorithms using waveform parameters for classifying open water and ice cover on northern lakes.

2.4 Concept of waveform parameterization

To characterize the altimetry waveforms, seven waveform parameters were extracted in this study: Leading Edge Width (LEW), Offset Center of Gravity (OCOG) Width, Pulse Peakiness (PP), backscatter coefficient (Sigma0), late tail to peak power (LTTP), early tail to peak power (ETPP) and the maximum value of the echo power (Max). These parameters are described below and shown schematically in Figure 2-9. Like other parameters, the peakiness of the waveform (i.e., how peaky the waveform is) is hard to pinpoint in the figure. Hence PP and the parameters based on peakiness, including LTPP and ETPP, are not labelled in Figure 2-9.

1) **Max** is the maximum power value of the echo waveform (Figure 2-9).
2) **LEW** is the distance between the first bin position containing equal to or greater than 10% of the power maximum and the bin position of the maximum waveform power (Figure 2-9).
3) **PP** is the ratio of the maximum power to the accumulated echo power. PP used in this study was defined by Ricker et al. (2014) as

$$PP = 128 * \frac{P_{max}}{\sum_{i=1}^{128} P_i} \tag{2.4}$$

where P_{max} is the maximum power in the echo waveform and P_i is the power in the i^{th} bin.

4) **OCOG Width** provides information about the width of the waveform, which is derived from the Offset Centre of Gravity retracker (OCOG) algorithm. Wingham et al. (1986) developed the OCOG retracker algorithm to calculate the waveform's centre of gravity (COG) by approximating the waveform with a rectangular box. The width of the rectangular box, which is the OCOG width, is computed as follows,

$$W = \left(\frac{\left(\sum_{i=1}^{128} {P_i}^2 \right)^2}{\sum_{i=1}^{128} {P_i}^4} \right) \tag{2.5}$$

where P_i is the power in the i^{th} bin.

5) **LTPP** is the ratio of the late tail to the peak power and is defined by (Rinne & Similä, 2016) as

$$LTTP = \frac{\frac{1}{21} * \sum_{i=\max+50}^{\max+70} P_i}{P_{max}} \tag{2.6}$$

where max is the bin position with maximum power, P_{max} is the maximum power in the echo waveform and P_i is the power in the i^{th} bin.

6) **ETPP** is the ratio of the early tail to the peak power and is defined by (Rinne & Similä, 2016) as

$$ETTP = \frac{\frac{1}{6} * \sum_{i=\max+1}^{\max+6} P_i}{P_{max}} \tag{2.7}$$

where max is the bin position with maximum power, P_{max} is the maximum power in the echo waveform, and P_i is the power in the i^{th} bin.

7) Unlike other waveform parameters, Sigma0 is delivered in the Synthetic Aperture Radar Altimeter (SRAL) L2 data product. It is computed from the returned power of the echo pulse by OCOG retracker algorithm.

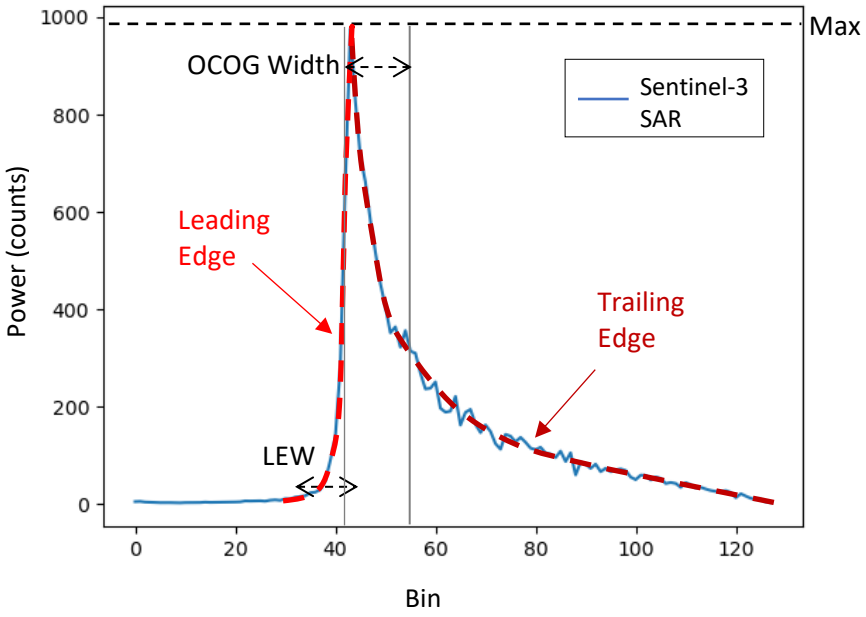

Figure 2- 9 Schematic visualization of different waveform parameters (Max, LEW and OCOG Width)

2.5 Limitations of past studies on lake ice from altimetry missions and contributions of thesis

Compared to sea ice studies, we have seen limited work on lake ice and using coarse resolution (~10-35 km) brightness temperature and LRM altimetry measurements. In addition, the only lake ice classification study based on the waveform parameterization concept (Ziyad et al., 2020) considered only a limited number of lakes to develop their classification algorithm (e.g., focused only on four lakes). Moreover, none of the studies used SAR altimetry data in their lake ice and open water classification algorithms. The coarser resolution brightness temperature measurements and LRM data limit the applicability of these approaches to very large lakes.

Recent investigations for sea ice have examined a larger set of waveform parameters (5-8) than for lake ice (1-3) and have also assessed several machine learning (ML) algorithms, obtaining accuracies between 75.37% to 91.83 % for FYI, 39% to 82.80% for MYI, and 88.26% to 93.87% for open water.

In this thesis, we draw from the important literature on sea ice to assess, for the first time, the use of waveform parameters from SAR altimetry, without the need for coarse-resolution brightness temperature data, and the evaluation of several ML algorithms to classify open water and ice cover at various stages of development and decay, beyond what has been published to date. The next chapter describes such advancement, including the parameterization of SAR waveforms, application of four ML algorithms and assessment of spatial cross-validation over the 11 study lakes.

Chapter 3

Machine Learning Based Classification of Lake ice and Open water from SAR Altimetry waveform features

3.1 Introduction

Lakes cover vast expanses of land at northern high latitudes and, therefore, play a key role in regulating weather and climate (Brown & Duguay, 2010). The lakes are ice-covered for several months of the year which makes them an important component of the cryosphere. As the physical, chemical and biological properties of lakes respond quickly to the changes associated with climate, lakes are considered effective sentinels of climate change. Lakes also have a significant impact on the northern communities since the presence (or absence), extent and thickness of lake ice affect transportation (ice roads), food security, recreational activities, and tourism in wintertime (Duguay et al., 2003; Adrian et al., 2009; Brown & Duguay, 2010). To acknowledge the importance of lakes for global climate monitoring, the Global Climate Observing System (GCOS) identifies them as Essential Climate Variables (ECVs); in particular, the attributes (or thematic products) are lake surface water temperature, lake extent, lake water level, lake ice cover, lake ice thickness and lake colour (water-leaving reflectance) (Belward et al., 2016; Buontempo et al., 2022). In the case of lake ice, in-situ observations of ice cover and its phenology (i.e., dates associated with freeze-up, break-up and ice cover duration) as well as lake ice thickness have significantly declined over the last three decades (Murfitt and Duguay, 2021). To deal with the erosion of in-situ observation networks in many northern countries, satellite remote sensing is assuming a greater role in the mapping and monitoring of lake ice (Duguay et al., 2015). Among the different sensor systems, passive microwave radiometers (Kang et al., 2012; Kang et al., 2014) and synthetic aperture radars (SARs) (Murfitt and Duguay, 2021) provide a viable means to monitor lake ice cover and lake ice thickness due to their capability of day/night acquisitions and under cloudy conditions.

Satellite altimetry is one of the radar remote sensing technologies that has shown great potential for the monitoring of lakes globally. Unlike imaging sensors, altimeters are profiling systems that collect data in the form of radar echoes along the earth's surface (i.e., tracks). Such radar echoes are recorded as a histogram of energy backscattered by the ground surface to the

satellite with respect to time; they are referred to as waveforms. Satellite altimetry has been used in hydrological and cryosphere applications for several years; however, little work has been conducted on lake ice compared to, for example, sea ice and the estimation of lake water levels (Birkett, 1995; Crétaux & Birkett, 2006; Kouraev et al., 2007; Sarmiento & Khan, 2010; Ricker et al., 2014; Zakharova et al., 2015; Gao et al., 2019). As altimetry is a well-established technique for water level monitoring, there exist several altimetry-based global water level databases, such as Hydroweb, G-REALM, and DAHITI as well the European Space Agency's (ESA) Climate Change Indicators (CCI) Lakes dataset which contains water level as one of the thematic products (Crétaux et al., 2011; Birkett et al., 2011; Schwatke et al., 2015; Crétaux et al., 2020). However, research is increasingly recognizing the presence of ice cover on lakes as a source of uncertainty in the retrieval of winter water levels (Birkett & Beckley, 2010; Sarmiento & Khan, 2010; Ricko et al., 2012; Shu et al., 2020a ; Nielsen et al., 2020). To address this issue, there is a need to develop approaches to classify surface conditions (open water and ice types) on lakes as to reduce errors or at least flag dates of the year when estimates of water level may be more uncertain. This is also true for the estimation of lake ice thickness (Beckers et al., 2017; Mangilli et al., 2022) where knowledge of surface conditions at the time of altimeter acquisitions would be useful. This is because current altimetry-based lake ice thickness (LIT) retrieval algorithms fail to provide accurate thickness estimates up until the young ice reaches a certain thickness (~ 0.26 m) or with surface melt (either episodic or generalized melt in spring) (Mangilli et al., 2022).

A limited number of studies have suggested approaches for the classification of lake ice and open water using data from satellite altimetry missions (Kouraev et al., 2007; Shu et al., 2020a; Ziyad et al., 2020). A threshold-based classification algorithm based on the combination of radar altimeter (backscatter coefficient) and multi-frequency (18 to 37 GHz) passive microwave radiometer (brightness temperature) observations from several LRM Ku-band altimetry missions (TOPEX/Poseidon, Jason-1, ENVISAT and Geosat Follow-On) complemented by SSM/I (Special Sensor Microwave/Imager) data has been proposed for discriminating between lake ice and open water in Lake Baikal (Kouraev et al., 2007). More recently, Ziyad et al. (2020) used the pulse peakiness (PP) values (derived from LRM radar altimetry waveforms) in addition to the backscatter coefficient (Ku-band) and brightness temperature values (average value from 18.7 GHz and 37 GHz measurements) of the Jason-2 mission to design a classification algorithm to discriminate between open water and different ice types (ice cover, ice freeze-up and ice break-

up) in the Canadian lakes (Great Slave Lake, Lake Athabasca, Lake of the Woods, and Lake Winnipeg). Using simultaneous brightness temperature (23.8 GHz and 36.5 GHz) measurements provided by the passive microwave radiometer aboard the Sentinel-3 satellite mission, Shu et al. (2020a) were able to detect the presence of ice in the lake as brightness temperature values are sensitive to the ice cover formation (Kang et al., 2012). Both Ziyad et al. (2020) and Shu et al. (2020a) developed classification approaches to improve the estimation of lake water levels from altimetry data as the presence of ice on lakes introduces biases in the water level estimates.

As mentioned above, only a few studies have proposed algorithms for the classification of lake ice types and open water from altimetry missions. However, a larger body of literature exists on the development and assessment of approaches for the classification of sea ice and open water. Most sea ice investigations propose the use of backscatter coefficients and parameters extracted from radar waveforms of the altimetry missions including high-resolution mode Cryosat-2 (Ricker et al., 2014; Wernecke & Kaleschke, 2015; Rinne & Similä, 2016; Shen et al., 2017a; Shen et al., 2017b; Shu et al., 2020b), Envisat (Müller et al., 2017), SARAL/AltiKa (Müller et al., 2017; Fredensborg Hansen et al., 2021) and Airborne Synthetic Aperture and Interferometric Radar Altimeter System (Zygmuntowska et al., 2013) to classify sea ice types and open water. All of these studies have achieved good overall classification accuracies (70.7% to >90%) for discriminating different sea ice types and open water, showing that the parameterization of waveforms provides great potential for discrimination between different sea ice types. This paper draws from the important body of work from the sea ice community by assessing several machine learning algorithms and waveform parameters to discriminate between different lake ice types and open water. Our study is the first one to apply the parameterization approach to SAR altimetry waveforms for lake ice cover classification.

The aim of the study is to evaluate the capability of different machine learning algorithms in classifying the lake surface conditions (open water and ice types) across ice seasons (freeze-up, ice growth and break-up periods) using waveform parameters and backscatter coefficients acquired by the radar altimeter aboard the Sentinel-3 satellite series from by the European Space Agency (ESA). To achieve this goal, the following objectives are set: 1) find the optimal combination of parameters to attain the best classification performance; 2) test the sensitivity of the classifiers to their internal hyperparameters; and 3) assess whether the classifiers' accuracies are affected by the spatial variation in the dataset or not from the selection of several lakes across the Northern

Hemisphere. The paper is organized as follows: Section 3.2 introduces the lake regions of interest and datasets used. It also describes the various classification algorithms tested. Section 3.3 presents the results and discussion, including the broader implications of the study. Finally, Section 3.4 summarizes the key findings and provides suggestions for future work.

3.2 Data and methods

3.2.1 Study area and altimetry data

Eleven lakes (Figure 3-1) distributed across the Northern Hemisphere were selected to train and evaluate several machine learning classifiers (see Section 3.2.4). The lakes are located in different geographical regions and experience a wide range of ice-cover conditions during winter. The selection of several lakes across different regions is meant to develop a classifier that is of global application. Table 3-1 lists the lakes considered in this study and some of their characteristics.

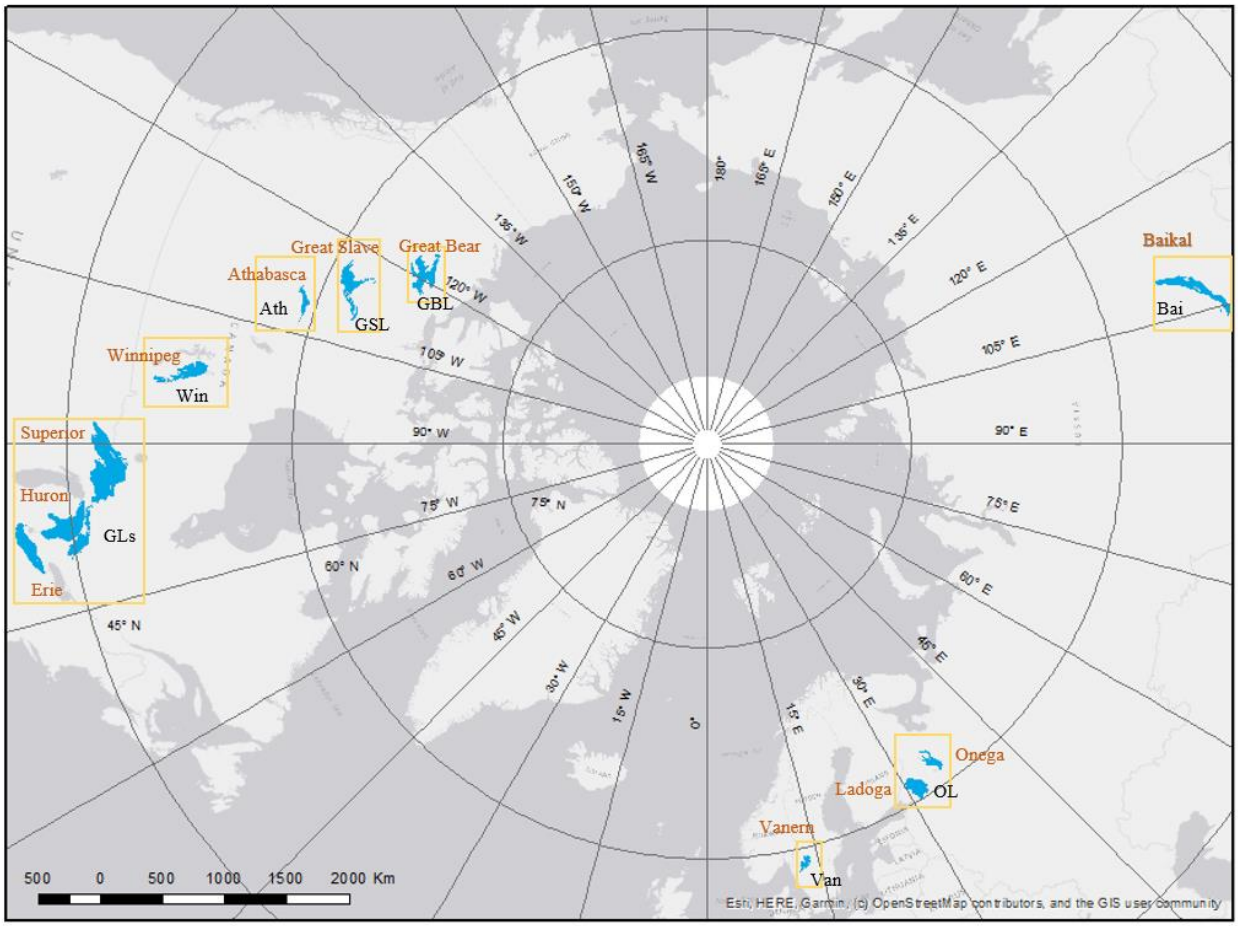

Figure 3- 1 Location of lakes selected for this study. Yellow rectangles with black labels indicate regions of spatial clusters (a lake or set of lakes in a specific region are grouped into a single cluster)

High-resolution Sentinel-3A/B level 2 SAR altimetry data acquired over three ice seasons (2018-2019, 2019-2020 and 2020-2021) were used in this study and downloaded from the CREODIAS platform (https://finder.creodias.eu/). CREODIAS is one of the five Data and Information Access Services (DIAS) online platforms that provide access to Copernicus data and information. The Sentinel-3 satellite series was developed by European Space Agency (ESA) as a part of the Copernicus programme. It consists of a constellation of two identical satellites: Sentinel-3A and Sentinel-3B launched on 16 February 2016 and 25 April 2018, respectively. The satellites are near polar sun-synchronous orbiting with an inclination of 98.65° and a repeat cycle of 27 days. One of the payloads of Sentinel-3 is a dual-frequency (C and Ku-band) radar instrument called synthetic aperture radar altimeter (SRAL), which measures in two modes, low-resolution mode (LRM) and SAR mode. In SAR mode, the SRAL instrument releases bursts of 64 Ku-band pulses surrounded by two C-band pulses and provides an along-track resolution of ~300 m. Only data acquired at Ku-band were used in this study.

Table 3- 1 List and characteristics of lakes selected for the study (Messager et al., 2016)

No.	Lake	Country	Latitude	Longitude	Elevation (m.a.s.l.)	Area (km^2)	Average depth (m)	Ice cover*
1	Athabasca	Canada	58.70	-111.20	207	7,528.73	20.6	Full
2	Baikal	Russia	52.23	104.32	449	31,967.85	738.7	Full
3	Erie	Canada/USA	42.90	-78.91	172	25,767.79	19.4	Partial
4	Great Bear	Canada	65.14	-123.51	145	30,450.64	72.2	Full
5	Great Slave	Canada	61.31	-117.62	148	26734.29	59.1	Full
6	Huron	Canada/USA	42.10	-82.42	175	59,399.3	59.8	Partial
7	Ladoga	Russia	59.95	31.03	-10	17,444.01	48	Partial
8	Onega	Russia	60.92	34.16	13	9,961.85	26.3	Partial
9	Superior	Canada/USA	46.47	-84.46	179	81,843.92	146.7	Partial
10	Vanern	Sweden	58.37	12.37	44	5,486.23	27.9	Intermittent
11	Winnipeg	Canada	53.70	-97.86	215	23,923.04	11.9	Full

*** Five of the lakes form a complete (full) ice cover, five form a partial ice cover (fractional coverage less than 100%), and one forms an intermittent ice cover (some portions of the lake form an ice cover but with multiple freeze/melt episodes that make the ice cover last for only a few days) in each winter.**

Previous studies have shown that altimetry observations are sensitive to land contamination (up to 2 km for SAR) and can influence the accuracy of the results (Liibusk et al., 2020). Hence, we excluded data points closer than 3 km from shorelines and islands to minimize the impact of reflections from land and land-to-water transition. The distance-to-land dataset produced by ESA's CCI Lakes project was used as the lake mask to delineate the study lakes (Carrea et al., 2015).

3.2.2 Auxiliary data

3.2.2.1 Satellite imagery

Imagery from optical and SAR sensors was used to collect sample data (i.e., training and testing set of the classifiers) along the altimetry tracks. For labelling, we collected samples through visual interpretation of Moderate Resolute Imaging Spectroradiometer (MODIS), Sentinel-2 Multispectral Instrument (MSI) and Sentinel-1 SAR images. Images used were captured either on the same date or within one day of Sentinel-3 SRAL acquisitions. The MODIS instrument on Aqua and Terra satellites covers the Earth's surface every 1-2 days, and more frequently at high latitudes, in 36 spectral bands from visible to thermal infrared wavelengths at 250 m, 500 m and 1000 m spatial resolutions. We used the corrected reflectance (true colour) product with 250 m spatial resolution obtained from https://worldview.earthdata.nasa.gov/. The Sentinel-2 mission has been providing a revisit period of 5 days with both A/B satellites in orbit since 2017. The MSI onboard Sentinel-2 acquires data in 13 spectral bands with a 12-bit radiometric resolution at 10 m, 20 m and 60 m spatial resolutions. The 10 m true colour imagery (MSI Level 1C) downloaded from https://scihub.copernicus.eu/dhus/#/home was used. Since optical imagery can be obscured by the presence of cloud cover, SAR imagery was also used to complement information provided from optical imagery. Sentinel-1 level-1 Ground Range Detected (GRD) SAR product was downloaded from Alaska Satellite Facility (https://asf.alaska.edu/) to further help with class labelling. The SAR images were processed using the Sentinel Application Platform (SNAP) software. The preprocessing procedure included the following steps: thermal noise removal, radiometric calibration, speckle removal (using a Refined Lee filter) and terrain correction.

3.2.2.2 Temperature data

ERA5-Land is a reanalysis dataset that offers global hourly estimates of a wide range of land climatic variables and is available at a spatial resolution of ~9 km (1950 to present). This study used the 2-m near-surface air temperature variable to determine the melting condition, i.e., whether the melting is happening or not. Since melting class labelling mainly relies on the ERA5 temperature measurements, it was ensured that the hourly timing of the sampled temperature and the observed timing of the altimetry data remains are nearly the same.

3.2.3 Method

In this paper, we distinguish open water and different lake ice types (open water, young ice, growing ice and melting ice) using satellite radar altimetry data and machine learning models (ML). The following flowchart (Figure 3-5) presents the main steps involved in the classification approach that was developed to classify different surface types of lakes.

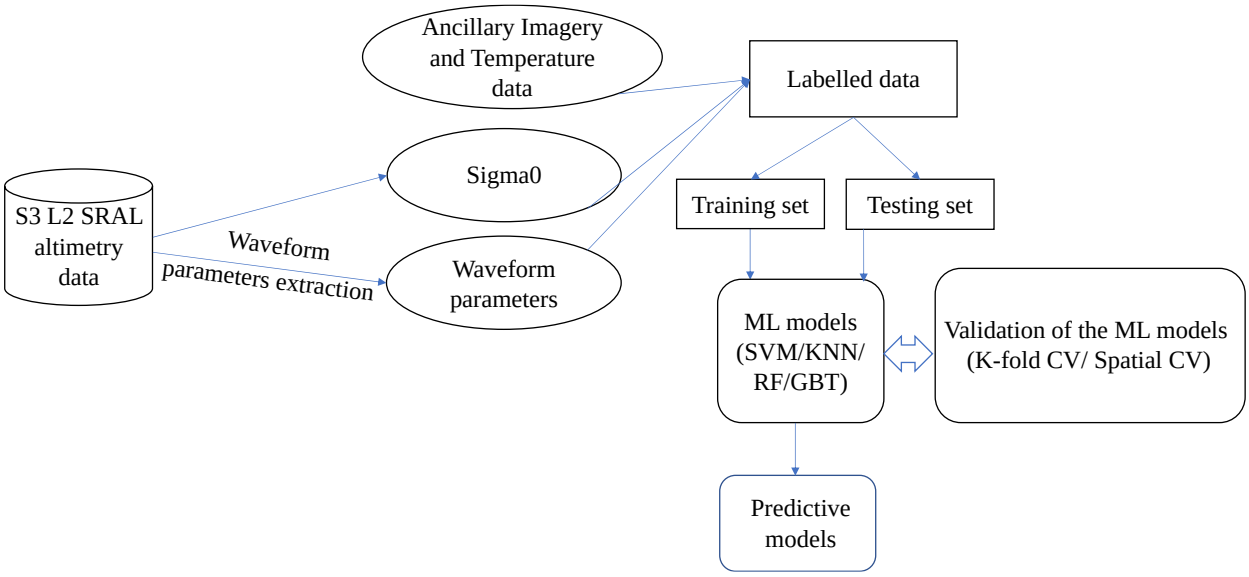

Figure 3- 2 Flowchart of processes performed to classify different surface types in the lakes.

3.2.3.1 Selection of waveform parameters

To characterize the altimetry waveforms, seven waveform parameters were extracted: the maximum value of the echo power (Max), Leading Edge Width (LEW), Pulse Peakiness (PP), Offset Center of Gravity (OCOG) Width, late tail to peak power (LTTP), early tail to peak power (ETPP) and backscatter coefficient (Sigma0). Figure 3-2 shows the schematic of a radar waveform labelled with some parameters (Max, LEW, TEW and OCOG_W) and parts of the waveform (Leading Edge and Trailing Edge). The following waveform-based parameters are extracted for the study:

1) **Max** is the maximum power value of the echo waveform.
2) **LEW** is the distance between the first bin position containing equal to or greater than 10% of the power maximum and the bin position of the maximum waveform power.

3) **PP** is the ratio of the maximum power to the accumulated echo power. PP used in this study was defined by Ricker et al. (2014) as

$$PP = 128 * \frac{P_{max}}{\sum_{i=1}^{128} P_i} \tag{3.1}$$

where P_{max} is the maximum power in the echo waveform and P_i is the power in the i^{th} bin.

4) **OCOG Width** provides information about the width of the waveform, which is derived from the Offset Centre of Gravity retracker (OCOG) algorithm. Wingham et al. (1986) developed the OCOG retracker algorithm to calculate the waveform's centre of gravity (COG) by approximating the waveform with a rectangular box. The width of the rectangular box, which is the OCOG width, is computed as follows,

$$W = \left(\frac{\left(\sum_{i=1}^{128} {P_i}^2 \right)^2}{\sum_{i=1}^{128} {P_i}^4} \right) \tag{3.2}$$

where P_i is the power in the i^{th} bin.

5) **LTPP** is the ratio of the late tail to the peak power and is defined by (Rinne & Similä, 2016) as

$$LTTP = \frac{\frac{1}{21} * \sum_{i=\max+50}^{\max+70} P_i}{P_{max}} \tag{3.3}$$

where max is the bin position with maximum power, P_{max} is the maximum power in the echo waveform and P_i is the power in the i^{th} bin.

6) **ETPP** is the ratio of the early tail to the peak power and is defined by (Rinne & Similä, 2016) as

$$ETTP = \frac{\frac{1}{6} * \sum_{i=\max+1}^{\max+6} P_i}{P_{max}} \tag{3.4}$$

where max is the bin position with maximum power, P_{max} is the maximum power in the echo waveform, and P_i is the power in the i^{th} bin.

7) Unlike other waveform parameters, Sigma0 is delivered in the SRAL L2 data product. It is computed from the returned power of the echo pulse by OCOG retracker algorithm.

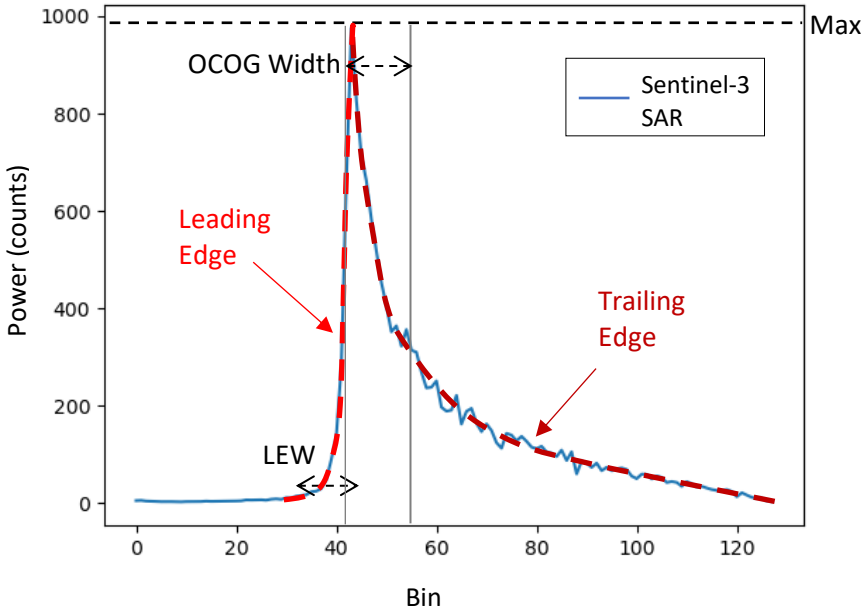

Figure 3- 3 Schematic showing parameters of the radar waveform

Four classes were considered in this study: 1) open water, 2) young ice, 3) growing ice, and 4) melting ice. Figure 3-3 shows an example of SRAL waveforms for each class.

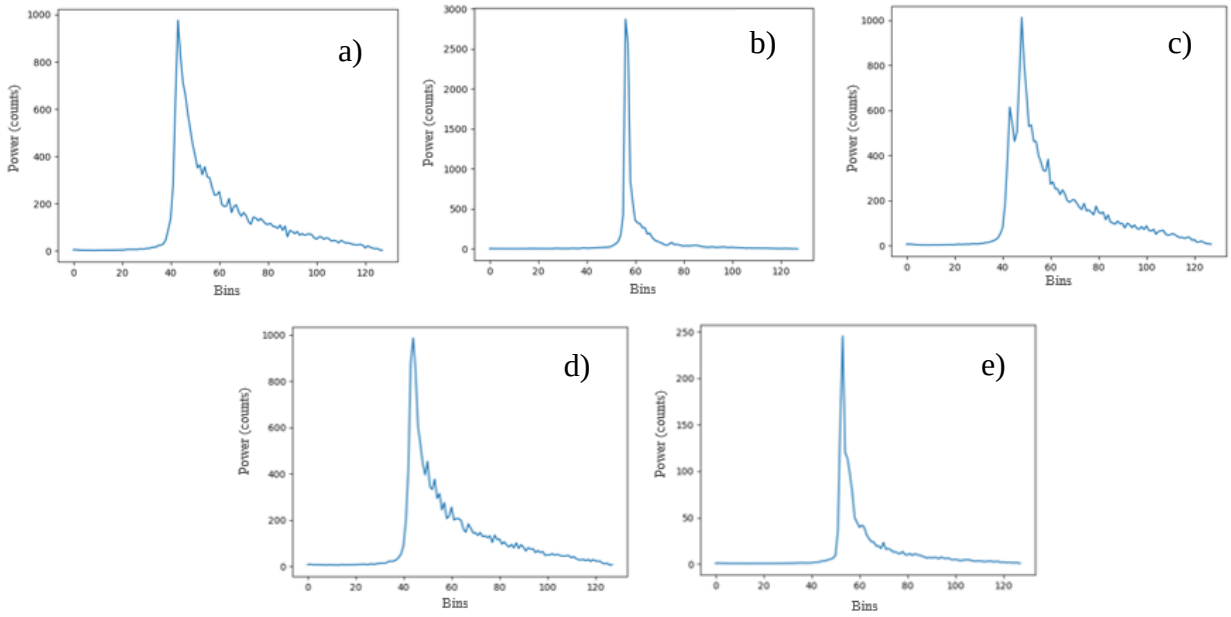

Figure 3- 4 SRAL waveform examples for a) open water, b) young ice, c) growing ice, d) melting ice and e) melting ice

Open water (OW) – Figure 3-3 a show the typical waveform shape of open water. The waveform of the open water can be easily identified as it has a single strong return (i.e., one peak) with a steep leading edge and a slowly decaying trailing edge. However, the presence of inhomogeneous surfaces (such as land area or a mixture of other surface types) within the altimeter footprint may lead to complicated shapes with many peaks.

Young ice (YI) – Skim (thin) ice formation in the lake at the beginning of freeze-up results in a sharp increase in backscatter coefficients. This sudden rise is due to the high reflectivity of newly formed ice. Thus, young ice is characterized by a high σ_0 value (Kouraev et al., 2007). The specular scattering of a mirror-like surface (thin/skim ice) produces a single narrow sharp peak (Figure 3-3 b). Hence, the backscatter coefficient values, and the shape of the waveform are considered for labelling an observation as young ice.

Growing ice (GI) – Beckers et al. (2017) and Mangilli et al. (2022) suggested that the double peaks on the leading edge of the altimetry waveform at the Ku-band represent the radar reflections from the snow-ice and ice-water interfaces. The authors proposed algorithms to estimate lake ice thickness using the bin distance between these two peaks. Thus, double backscattering on the leading edge of waveforms is indicative of ice growth and thus labelled as growing ice (Figure 3-3 c).

Melting ice (MI) – Ice and overlying snow cover experiencing melt was categorized as melting ice. Since it is hard to recognize a melt event using optical data alone, ERA5 temperature data was used to assist in the labelling of melting ice. If the 2-m height air temperature above the lake surface during the ice season is greater than 0 °C, it is labelled as melting ice. In a few cases where the melt was apparent from altimetry waveform and in SAR imagery, a lower threshold limit of the temperature was extended to -5 °C (Wiese et al., 2015). Unlike the other surface types, melting ice has no unique altimetry waveform shape. If there is any melting ice, the altimetry signal will show either open water (Figure 3-3 d) or young ice (Figure 3-3 e) waveform shape. Although melting ice waveforms look similar to Figure 3-3 a or Figure 3-3 b, the backscatter value range differs which helps to identify MI from other classes. Based on the visual assessment of altimetry

waveforms and auxiliary satellite images, it has been known that the melting ice usually gives off a young waveform shape (when there is little or no snow on the melting ice). Only during the initial melting stage is the open water waveform shape observed.

3.2.3.2 Variation in waveform parameter values on different surface types

Depending on the surface type of the lake, the signal reflected from it gives off different echo shapes. Thus, the waveform parameters' and backscatter coefficient values derived from such echo also vary. Waveform parameters including Max, ETPP and LTPP were eliminated from the subsequent analysis. The poor contribution of Max and ETTP parameters to the classification performance, evident through the feature importance chart (not shown), results in the elimination of the two parameters from the study. As we aim to develop an optimal classification algorithm which effectively classifies all four surface types (open water, young ice, growing ice and melting ice), we removed the LTPP parameter as Eq. 3.3 fails to estimate LTPP values over young ice. However, LTPP was found to be useful for distinguishing other surface types (except young ice). Figure 3-4 shows an example of the variability in waveform parameters and Sigma0 values over different surface types (open water, young ice, growing ice and melting ice). As expected, Sigma0, PP, LEW, and OCOG_W values have different value ranges across the different surface types, showing their capability to discriminate between different surface types. Compared to other waveform parameters, Sigma0 values are unique and have substantial value range differences when the echoes bounce off from open water, young ice, growing ice and melting ice. Similar to Kouraev et al. (2007), we also observe very high Sigma0 values (greater than 60 dB) for the young ice class. As young ice starts to grow, Sigma0 values decrease gradually until the melt onset. This agrees with the study conducted by Kouraev et al. (2007) and Kouraev et al. (2008) which reported that ice growth and snow accumulation on the ice induce a decrease in backscatter coefficient values.

During the early melt onset, an abrupt decrease (less than ~22 dB) in Sigma0 is observed, especially on the ice with the presence of snow on the top of the surface. Following this, Sigma0 continues to fluctuate over the melt period before stabilizing at the end of this stage. This fluctuation may be due to the rapid melting and refreezing events, formation of melt ponds on the lake surface, effects of rainfall, wind and loss of snow on the ice surface. Less absorption of the altimetry signal occurs at the lake surface when there is less or no snow. Interestingly, Sigma0

reaches a maximum value greater than ~60 dB amidst the value fluctuation phase during melt. Previous studies have also noticed such variability in backscatter coefficients during the break-up (Kouraev et al., 2007; Ziyad et al., 2020).

Melting snow or the presence of meltwater on ice limits the penetration of the radar signal; thus, the surface scattering dominates during this period. This explains the transition of double peak (growing ice) to single peak waveform once the melt starts. Additionally, at the early stage of melt, melt ponds form on the lake ice surface which is confused as the open water by the altimetry observation. This confusion happens as the current processing techniques of the radar altimeter data make it difficult for the altimeter to distinguish the melt pond from open water (Tilling et al., 2020). This suggests why one of the melting ice classes has an open water waveform shape (Figure 3-3 d).

During the open water period, all the waveform parameter values are stable; however, Sigma0 values are in two different value ranges (23-27 dB or 45-48 dB). The reason may be due to the influence of wind during the Sentinel-3 acquisitions. Overall, the variations in PP are similar to Sigma for all surface types except open water. This behaviour is clearly visible in Figure 3-4. Like Sigma0, PP reaches maximum values in the first (young) ice formation stage.

a)

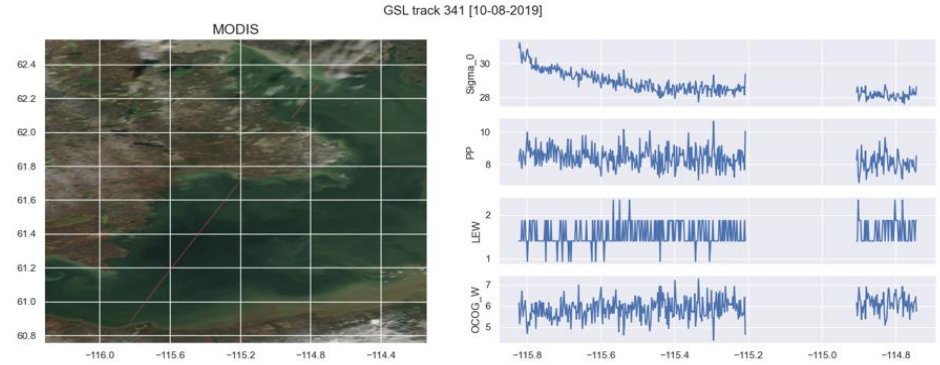

b)

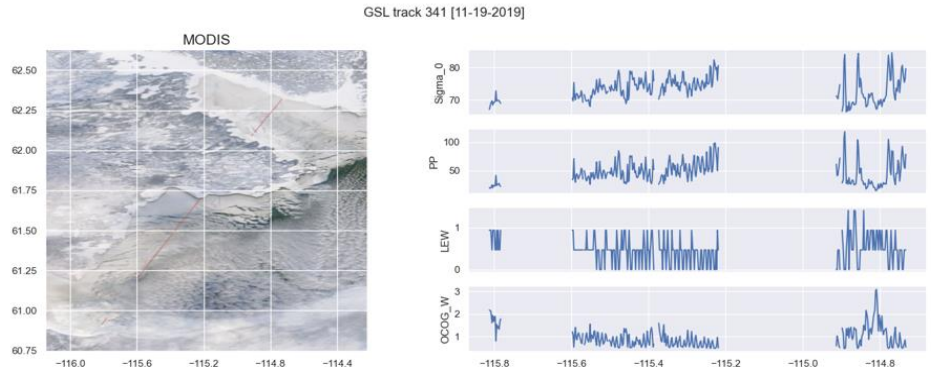

c)

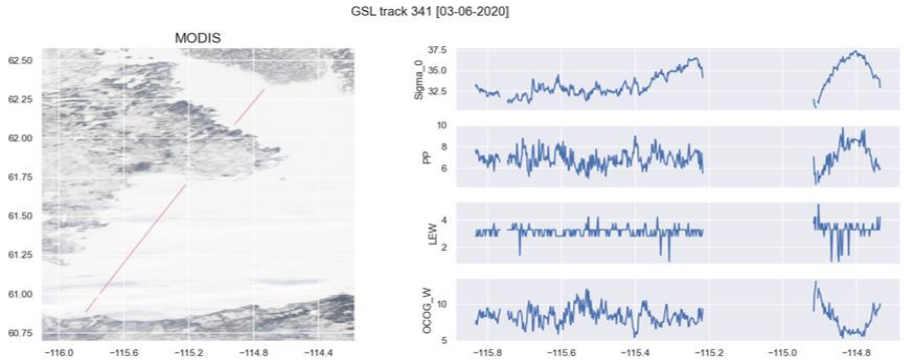

d)

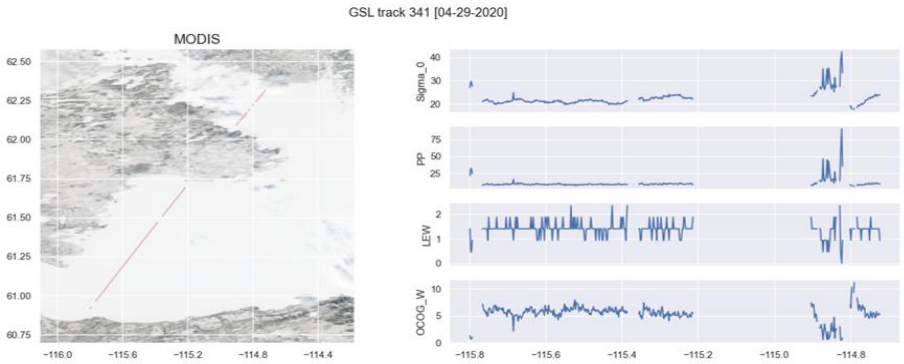

Figure 3- 5 Evolution of the waveform parameter values along Sentinel-3 track 341 on Great Slave Lake during the stages of a) open water, b) young ice, c) growing ice, and d) melting ice

3.2.4 Classifiers

To perform the classification of lake ice types and open water with different configurations of waveform parameters, four ML algorithms were evaluated: Support Vector Machine (SVM), K Nearest Neighbours (KNN), Random Forest (RF) and Gradient Boosting Trees (GBT). The details of each classifier and associated hyperparameters are described below. All four classifiers were implemented using the scikit-learn package in python. The following classifier functions of the package were used: svm.SVC (SVM), neighbors.KNeighborsClassifier (KNN), ensemble.RandomForestClassifier (RF), and ensemble.GradientBoostingClassifier (GBT).

Support Vector Machine (SVM) is a simple machine learning algorithm commonly used in classification problems. The main focus of SVM is finding an optimal hyperplane in N-dimensional space (N- the number of features) that distinctly segregates the data points into different classes. The data points closer to the hyperplane are called support vectors, which influence the position and orientation of the hyperplane. SVM, in general, is a linear classifier.

However, the kernel function in SVM can perform a non-linear classification by transforming the low-dimensional space into a higher-dimensional space where the data points can be linearly separable. The radial basis function (RBF) kernel was used in SVM to handle the non-linear problem. In addition, the hyperparameters, including Cost and Gamma, were tuned to achieve the best accuracy. Cost is a regularization constant, and Gamma is the kernel width of the RBF.

The K Nearest Neighbours (KNN) classifier uses the proximity of the data points to perform classification, i.e., if any data points are close to each other, then they belong to the same class. Thus, the distance metric acts as a decision boundary that classifies the data points. The distance metric used in KNN is Manhattan distance which calculates the distance between two real-valued vectors. The hyperparameters considered for tuning the KNN classifier are n_neighbours (the number of proximity neighbours) and leaf_size (the minimum number of data points in a node).

Random Forest (RF) is an ensemble method that generates a large number of decision trees to make predictions. In each decision tree, samples are selected randomly from the original dataset with replacements called Bootstrapped datasets. This bootstrapping approach ensures that not all decision trees have the same sample, making the model less sensitive to the original dataset. Moreover, features are also selected randomly during the construction of decision trees to reduce the correlation between the trees. Each decision trees make predictions, and the final result is decided based on the majority voting. This process of combining results from multiple models is called Aggregation. Such randomness created from Bootstrap Aggregation (or Bagging) and random feature selection helps to limit overfitting in Random Forest. The number of decision trees that need to be built before taking the majority voting (n_estimators) and the number of features that need to be considered for the best split (max_features) are the two hyperparameters used to tune the RF classifier.

Gradient Boosting Trees (GBT) is another ensemble method that falls under the category of boosting algorithms. Unlike RF, in this classifier, decision trees are connected sequentially. The objective of GBT is to minimize the errors of the previous model, thereby developing a robust model. GBT achieves it by iteratively learning from each of the weak learners and updating the weights of the wrongly classified data points before feeding them into the next model. The hyperparameters used in GBT are n_trees (number of decision trees) and lr (learning rate).

Waveform features and backscatter coefficients extracted from the SAR altimetry waveforms were used as the sample data for the ML classifiers. Each sample was categorized under open water, young ice, growing ice and melting ice classes described earlier. Manual class labelling based on Sentinel-3 SRAL waveforms and complementary satellite imagery (Sentinel-1 imaging SAR, Sentinel-2 MSI Level 1C data, and MODIS Aqua/Terra) was performed to create training and test samples for the classifiers. For each lake, samples of all four classes (wherever available) were collected for the period 2018-2021 (i.e. three ice seasons). The collected samples consisted of 104,558 waveforms (open water: 29,131, young ice: 22,258, growing ice: 25,920, and melting ice: 26,249), of which 80% and 20% were used as training and testing sets, respectively, for the classifiers. Figure 3-5 presents the methodology of the classification approach to discriminate between open water and lake ice types.

3.2.5 Feature Importance

Feature importance helps in finding the waveform parameters crucial for correctly classifying the surface type classes of the lake. Here, the permutation-based variable importance approach (PBVI) was applied to calculate the importance of each waveform parameter. The PBVI estimates and ranks the feature importance based on the model's prediction error increase when a feature value is randomly permuted. To implement the PBVI method, the permutation_importance function in sklearn's inspection package was used in this study (Wu et al., 2021).

3.2.6 Validation Approaches

The accuracy score of each classifier is considered as a measure to evaluate the classification performance. A classifier may perform well with a specific dataset but not with any unseen or additional dataset. Thus, one needs to guarantee that the model works well with any new samples and is not refined to the specific training samples. Hence, two strategies were implemented to ensure the model's efficacy and reliability. One is the random k-fold cross-validation (CV) method to calculate the overall accuracy of the classifier. In k-fold CV, the total dataset is split into k number of subsamples called folds of equal sizes. Then, a single subsample is validated against the model developed with k-1 subsamples until each subsample is used as a testing set at least once.

Another validation strategy, Spatial CV, was implemented to examine the classifier's capability to cope with the spatial heterogeneity in data. In this approach, the training and testing sets are resampled from the whole dataset based on the spatial information attached to each sample. Lakes geographically close to each other are considered a single cluster; hence, herein, 11 lakes are grouped into 8 clusters (Table 3-2). In accordance with this method, this strategy is similar to a k-fold CV, except that each cluster represents each fold. The two validation approaches helped to carry out a bias-reduced assessment of the classifier's predictive performance and, thus, assisted in avoiding overfitting.

Table 3- 2 The clusters of spatial CV

Clusters	Lakes
Ath	Lake Athabasca
Bai	Lake Baikal
GBL	Great Bear Lake
GLs	Lake Superior, Lake Huron, Lake Erie
GSL	Great Slave Lake
OL	Lake Onega, Lake Ladoga
Van	Lake Vanern
Win	Lake Winnipeg

3.3 Results and discussion

3.3.1 Comparison of parameter combinations

Seven waveform parameter configurations were considered to examine the variation in the classifier's performance with different configurations and to find the optimal parameter combination for classifying open water and different lake ice types with ML classifiers. Since some studies on lake ice (and sea ice) and open water classification have shown that Sigma0 is a significant parameter for distinguishing surface types, it is included in all parameter configurations (Kouraev et al., 2007; Shen et al., 2017a, Shen et al., 2017b, Tilling et al., 2018; Ziyad et al., 2020). As Figure 3-6 shows, the overall accuracy of the classifiers improves in the parameter

configurations with three or more waveform parameters. However, the overall accuracy is not consistently increasing with the addition of more parameters. For instance, the mean accuracies of the 7-parameter configuration in all classifiers are lower than the three and four parameter configurations. Compared to other combinations, the mean accuracies of the Sigma0 + PP + OCOG_W + LEW combination are high (95.46% - 95.88 %) across all classifiers. In addition, the interquartile range of the boxplots for this combination are relatively very less (short box length), suggesting that the overall accuracies obtained by different folds of the 10-fold CV are close to each other (less variation in the accuracy values). Hence, it is found that the Sigma0 + PP + OCOG_W + LEW combination is the optimal parameter configuration and is therefore used to implement for all subsequent analyses.

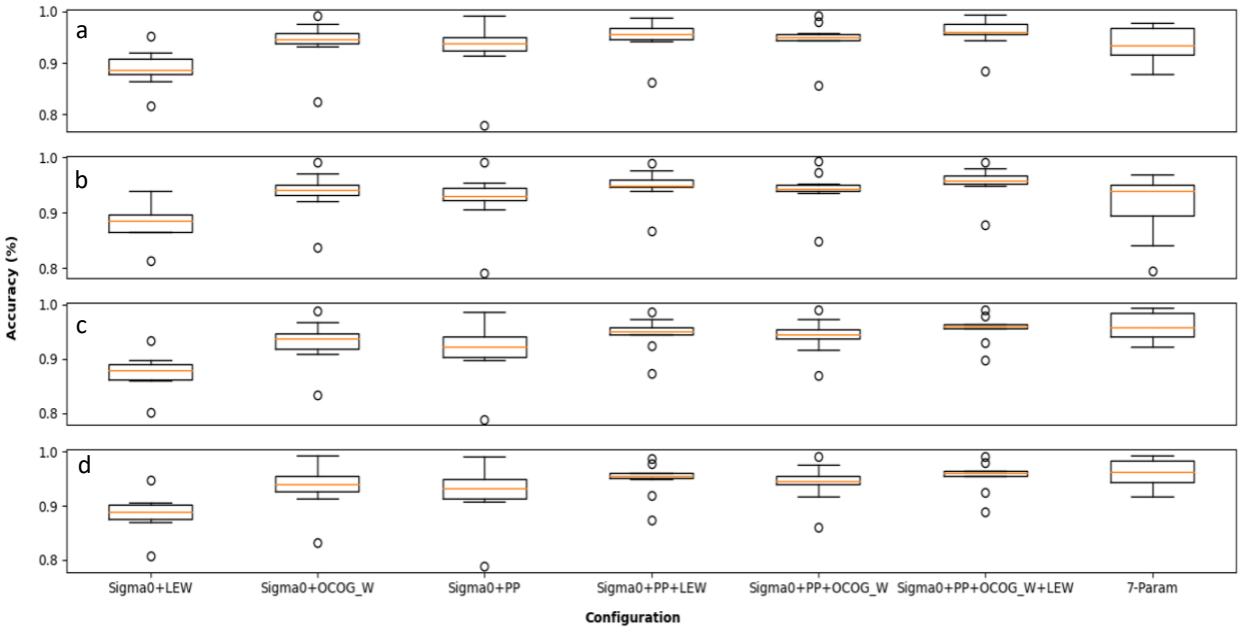

Figure 3- 6 Overall classification accuracies achieved with a) SVM, b) KNN, c) RF and d) GBT for different waveform parameter combinations

Figure 3-7 shows the permutation-based feature importance (PBVI) values of the most important parameters for each classifier. For all four classifiers, Sigma0 has a very high feature importance, followed by OCOG_W and PP. LEW is the least significant parameter contributing

to the classification's performance. The OCOG_W remains the second most important parameter in three of the four classifiers, suggesting that OCOG_W has comparable capability in discriminating the lake ice (young ice, growing ice and melting ice) and open water classes.

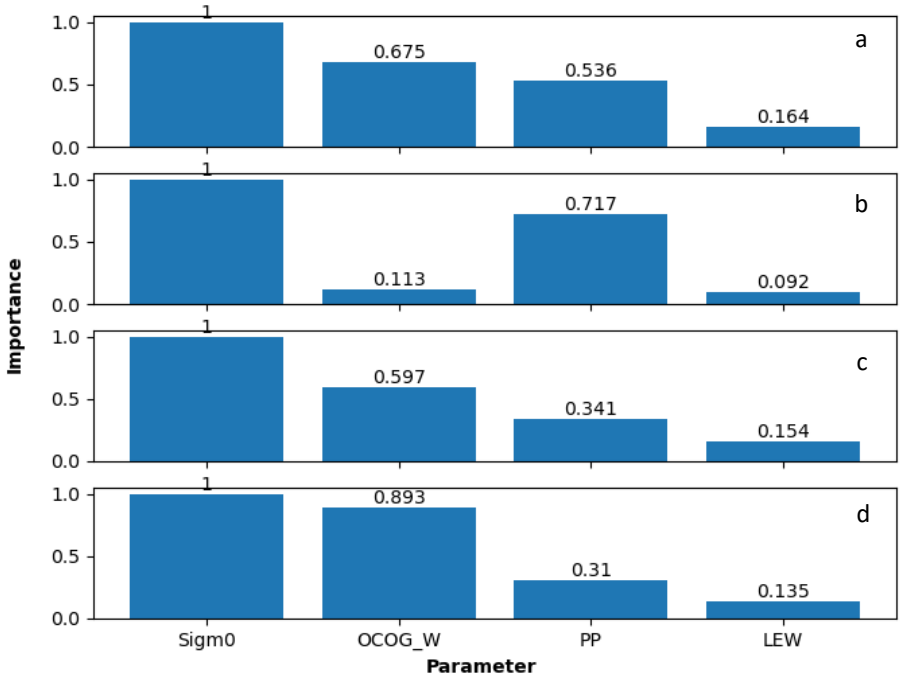

Figure 3- 7 Comparison of parameter importance obtained by permutation-based variable importance for a) SVM, b) KNN, c) RF and d) GBT classifiers

3.3.2 Sensitivity analysis of hyperparameters

The hyperparameters of each classifier were tested with different values to examine their influence on classification accuracy. The GridSearchCV function in the sklearn's model selection package with a 10-fold setting was used to perform the sensitivity analysis of hyperparameters and to determine the best parameters that provide the best classification accuracy. Table 3-3 shows the testing values of hyperparameters and the best ones for each classifier. Figure 3-8 shows how much the classification accuracies of the four classifiers vary when trained with different hyperparameter values. The accuracy scale on all plots is set to the same limit to provide a better visual comparison.

As shown in Figure 3-8 a, SVM is sensitive to its two key hyperparameters, Cost and Gamma. A small value of Cost and Gamma results in a lower accuracy of 91.68%. However,

training with a high value of Gamma combined with a high value of Cost also results in a slight drop in classification accuracy. SVM is less sensitive to Gamma than Cost with the former providing relatively stable classification accuracies (95.3% - 96.14%) at 0.01 and 0.1. Fig 3-8 b shows the classification accuracy of the KNN classifier by varying n_neighbors and leaf_size at p=1. From this figure it is clear that the KNN's accuracy does not vary greatly with a change in hyperparameter values. Classification accuracy remains stable across a range of values of the hyperparameters. Hence, the KNN classifier is less sensitive to hyperparameters.

In the case of RF, the classifier's performance is less affected by the hyperparameter values (Figure 3-8 c). For RF accuracies range between 95.83% and 95.88%. Since using a large number of decision trees (n_estimators) demands more computational power and running time, 500 trees were used. Figure 3-8 d illustrates the sensitivity of the GBT classifier to the hyperparameters. With a high learning rate (lr=0.1), the number of decision trees (n_trees) does not influence the classifier's overall performance. However, smaller learning rate (lr=0.01) combined with a small number of trees (n_trees =50, 100) significantly impact accuracies by leading into a large drop from ~95.5% to ~92%.

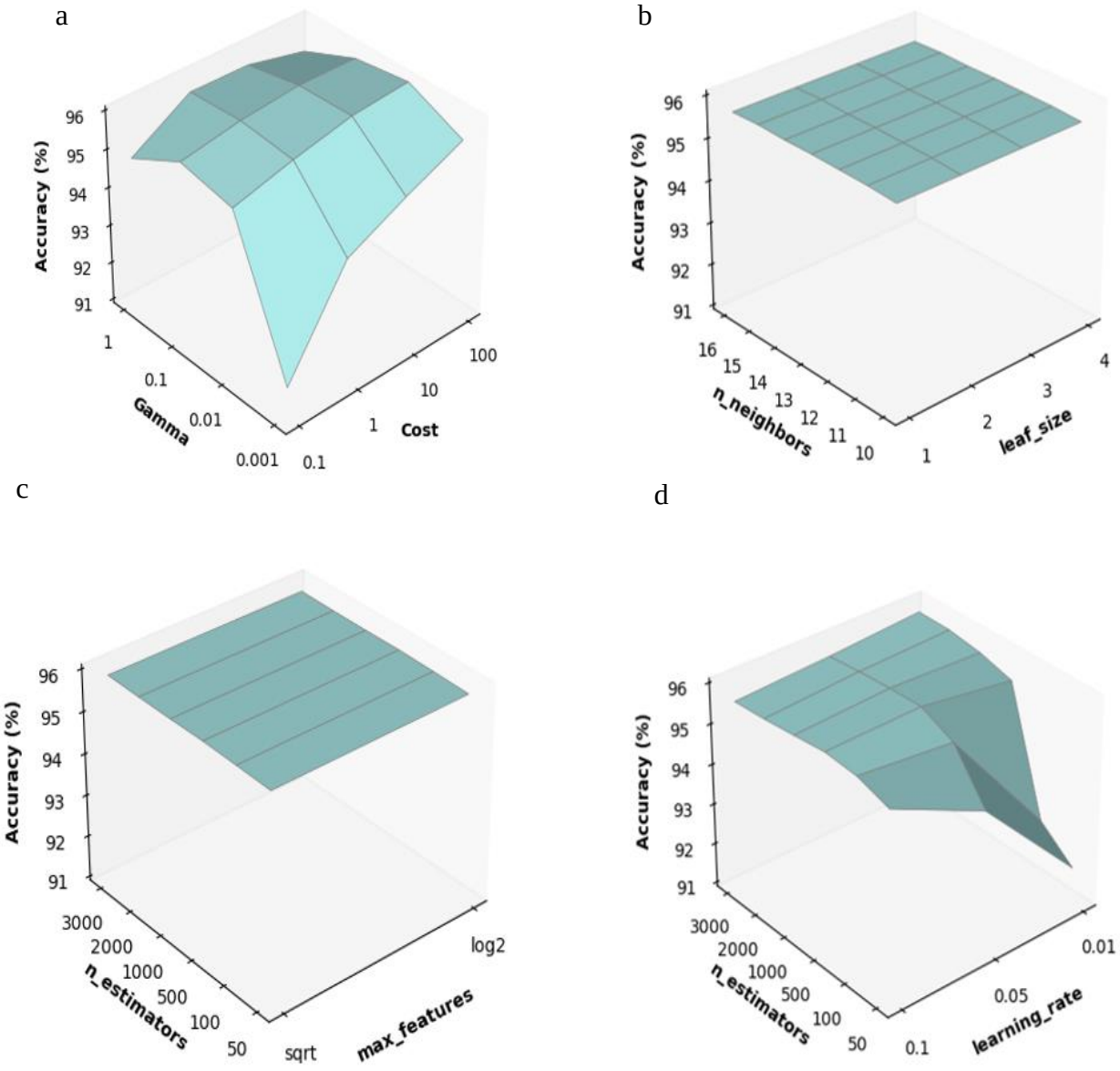

Figure 3- 8 Comparison of classification accuracies with a change in hyperparameter values for a) SVM, b) KNN, c) RF and d) GBT

Table 3- 3 Classifiers with hyperparameters tested in sensitivity analysis

Classifier	Hyperparameter & its testing values	Best hyperparameter
SVM	C: 0.1, 1, 10, 100 Gamma: 0.001, 0.01, 0.1, 1	C = 100 Gamma = 0.01
KNN	leaf_size: 1, 2, 3, 4 n_neighbors:10, 11, 12, 13, 14, 15, 16	leaf_size = 1 n_neighbors = 15
RF	n_estimators: 50, 100, 500, 1000, 2000, 3000 max_features: sqrt, log2	n_estimators = 500 max_features = sqrt
GBT	n_trees: 50, 100, 500, 1000, 2000, 3000 learning_rate: 0.1, 0.05, 0.01	n_estimators = 500 learning_rate = 0.05

3.3.3 Spatial transferability assessment

Results of the spatial assessment carried out on the spatial clusters (Table 3-2) are summarized in Table 3-4. Interestingly, all four classifiers achieved a comparable mean accuracy, which indicates that they all performed well across the clusters and did not suffer much from spatial variation. Classification accuracies above 90% were achieved for all clusters except Vanern. The poorer classification performance at Lake Vanern may be due to its irregular and compact shoreline structure. Such sheltered lakes do not form high waves and are easily subjected to land contamination which could affect the altimetry waveform shape, even if care was taken to create lake buffers to eliminate this effect prior to classification. The high accuracy consistency across the clusters suggests that the waveform parameter-based classification approach possesses good spatial transferability and that it could likely achieve high accuracies if applied to other lakes of the Northern Hemisphere that form a seasonal ice cover.

Table 3- 4 Spatial CV accuracy of the lake clusters across all classifiers

Clusters	SVM (%)	KNN (%)	RF (%)	GBT (%)
Ath	94.88	94.5	95.08	95.09
Bai	97.86	97.74	97.74	97.9
GBL	97.85	97.95	97.51	97.31
GLs	95.59	92.51	91.08	92.59
GSL	94.23	94.06	94.87	94.61
OL	99.02	98.59	98.47	98.60
Van	86.66	84.9	83.58	83.87
Win	92.48	89.98	92.51	91.87
Mean accuracy	**94.82**	**93.78**	**93.86**	**93.98**

3.3.4 Surface type predictions along altimeter tracks

Figure 3-9 shows prediction results of the four classifiers for the different surface types (growing ice, melting ice, young ice and open water) along Sentinel-3 altimeter track 346 over Great Slave Lake. Figure 3-9 a shows the prediction results obtained during freeze-up on GSL (November 21, 2017). Unlike the other examples, Figure 3-9 a presents two main surface types along the track: young ice and open water. On the MODIS image, young ice is visually easier to identify compared to open water which is largely covered by fog or low-level clouds. Although the young ice and open water classes are predicted well, there are some misclassifications too. It is important to note that the location of these misclassifications occurs at the transition from young ice to open water and vice-versa along the track. This implies that the altimetry signal is affected by ice presence even though areas occupied by ice are not situated directly under the nadir viewing angle of the altimeter but in the vicinity. Compared to other classifiers, RF performed best and correctly predicted the growing ice class without any misclassification on March 23, 2017 (Figure 3-9 b). The other classifiers predicted the growing ice class also relatively well with a few classification errors. As shown in Figure 3-9 c, the majority of the prediction results correspond to melting ice (May 16, 2017) while a few are incorrectly classified as growing ice. It is worth noting

that all classifiers predict growing ice almost at the same locations, which are near or on pressure ridges formed on the ice surface (see bright areas of underlying MODIS image in Figure 3-9 c). This pattern indicates that the altimetry signals are sensitive to deformation features such as pressure ridges and that the classifiers are good at recognizing the different (or complex) waveform shapes. Since there is no specific class for ridges, our classification approach tried to accommodate the different waveforms by categorizing them under a class (Growing ice) with shapes closely like them. This may be the reason as to why most of the other classes in Figure 3-9 c are growing ice. It is clear from the along-track spatial analysis that most of the misclassifications shown in Figure 3-9 occurred due to the complex-shaped waveforms (look similar to waveforms in Figure 3.3 but with additional peaks and/or step like feature) over transition areas or in the presence of ridges on the lake ice surface.

a)

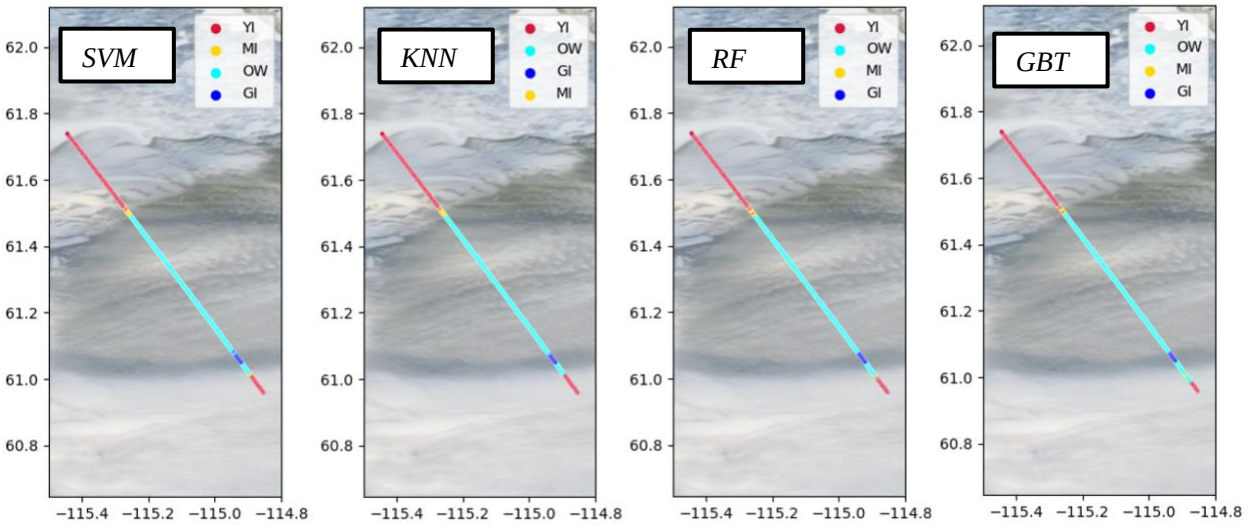

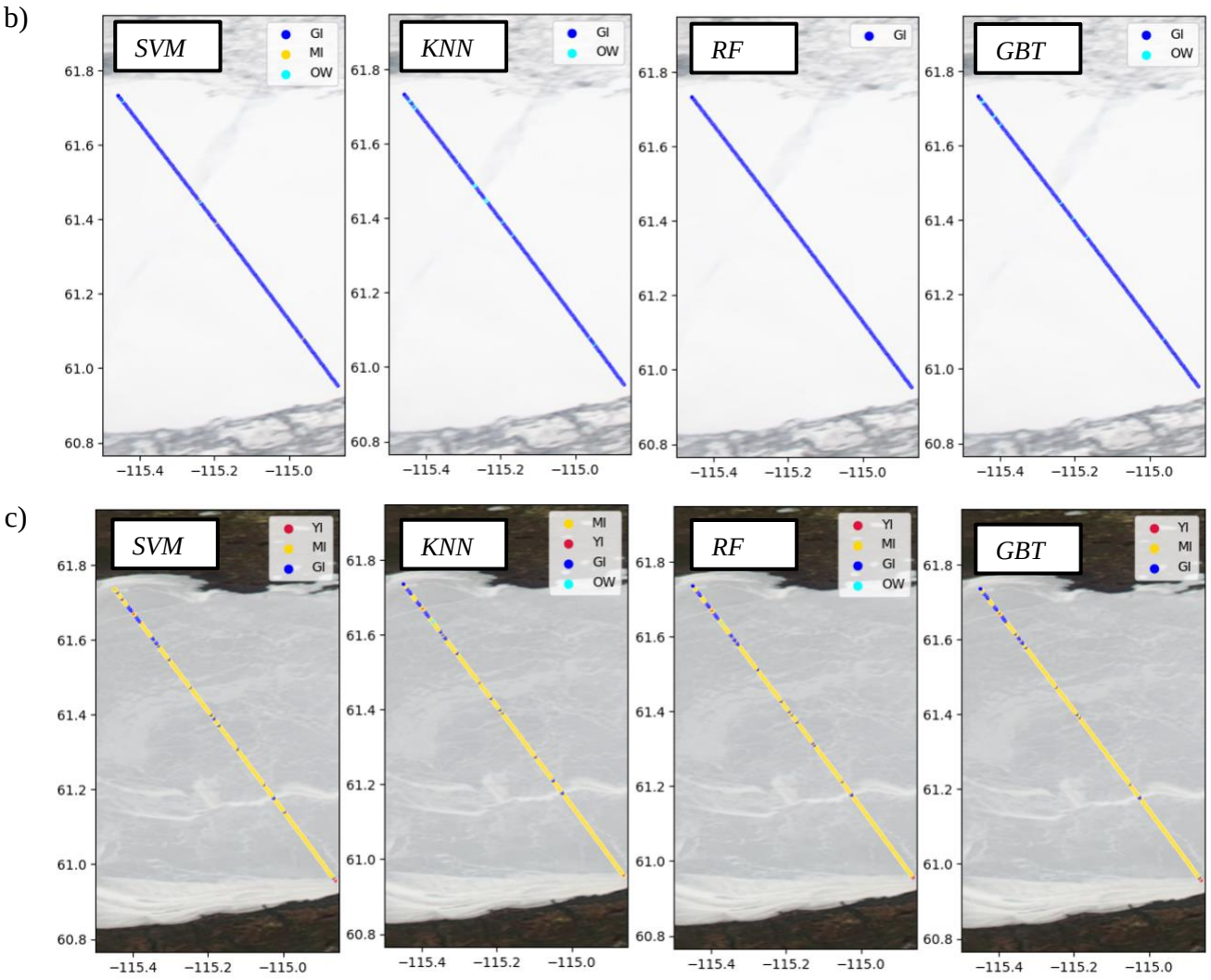

Figure 3- 9 Prediction results of different surface types, including a) Young ice, Open water [November 21, 2017], b) Growing ice [March 23, 2017], and c) Melting ice [May 16, 2017] and. The Sentinel-3 altimeter track 346 is overlaid on MODIS images acquired on the same day or within one day

3.3.5 Implications of classification results for the retrieval of ice thickness and lake levels

The satellite radar altimetry technique acts as a basis for creating many water level datasets and has a long history of utilization for the estimation of lake water levels. However, only recently have researchers started to recognize that the presence of ice on lakes introduces errors in

calculating the surface height, which affects water level retrievals (Birkett & Beckley, 2010; Sarmiento & Khan, 2010; Ricko et al., 2012; Shu et al., 2020a; Nielsen et al., 2020). To improve existing water level estimation approaches or to develop a new lake level retrieval method, identification of surface type (various ice classes and open water) would be beneficial to flag surface conditions and associated dates when the quality of retrievals may be highly uncertain. With knowledge of surface type, for example as to whether altimeter observations are over lake ice or not, researchers could choose to either eliminate such error-inducing measurements (Ziyad et al., 2020) or to estimate an equivalent water level (Shu et al., 2020a).

In addition to discriminating between lake ice and open water, the classification algorithms presented herein did well at distinguishing between different ice types (young ice, growing ice and melting ice). Such information would be helpful for identifying times when lake ice thickness retrievals may be limited or not possible. Current algorithms based on altimetry data fail to provide reasonable thickness estimates with the start of melt onset in spring and during the early stage of ice formation in fall/winter. For example, Mangilli et al. (2022) developed a new retracker called LRM_LIT to retrieve the lake ice thickness (LIT) from Jason-2/3 LRM radar altimetry (Ku-band) data. Compared to previous studies, the retrieval approach developed by Mangilli et al. (2022) offers a significant improvement for the estimation of LIT (~0.10 m accuracy once the lake ice cover is well established and prior to melt onset). The method is currently being implemented as part of ESA's CCI+ Lakes project to generate LIT time series. However, the LIT retracker cannot estimate LIT precisely when the lake ice is too thin due to range resolution and when the snow on ice begins to melt.

Figure 3-10 shows the LIT analysis carried out for the 2015-2016 ice season at Great Slave Lake by Mangilli et al. (2022). It is clear from this figure that the LRM_LIT retracker-based ice thickness estimates are close to those obtained with a numerical lake ice model (Duguay et al., 2003) and in-situ thickness measurements except during the initial days of freeze-up and after melt onset. The waveform parameter-based classification algorithms could, for example, be used as part of a pre- or post-processing step to flag surface conditions along with dates under which LIT retrievals may be least and more uncertain.

Most of the available altimetry data are in LRM, while the classifiers evaluated in this paper were based on the processing of high-resolution SAR altimetry data. Thus, further work is

needed to explore the potential of transferring the waveform parameter-based classification method to LRM altimetry data.

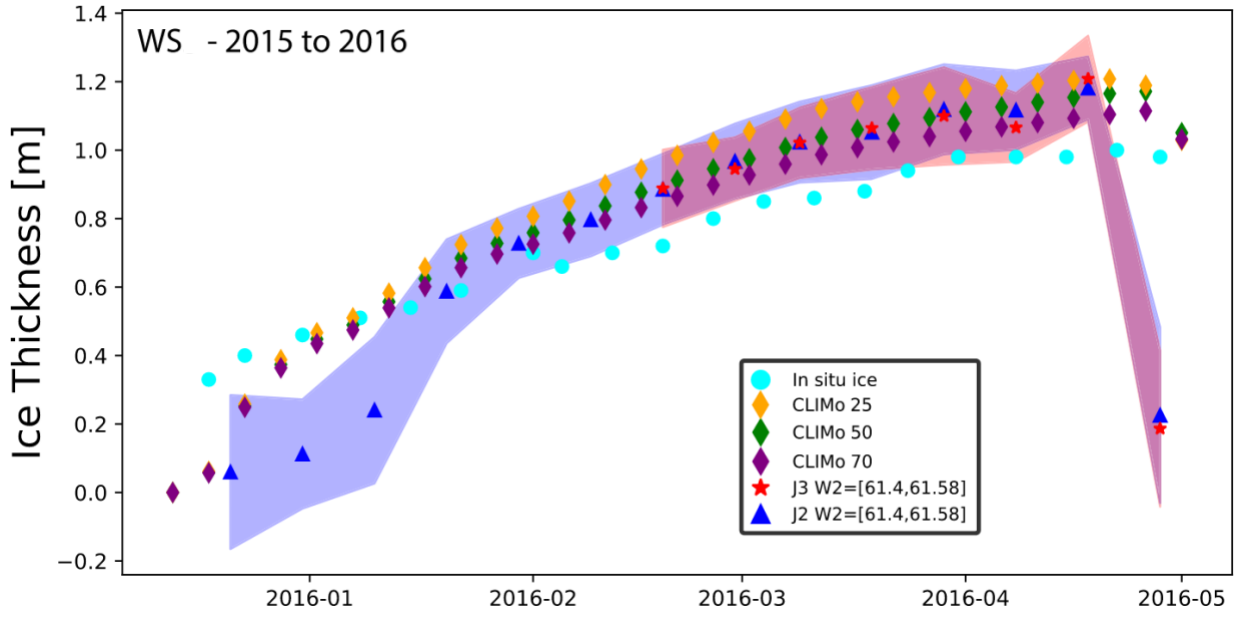

Figure 3- 10 Comparison between lake ice thickness estimates over GSL (2015-2016 winter) from Jason-2 (triangles) and Jason-3 (stars), CLIMo simulations with varying amounts of snow on ice (diamonds) and in-situ measurements from Black Bay (circles) (Source: Mangilli et al., 2022)

3.4 Conclusions

This study assessed four ML algorithms applied to SAR altimetry measurements for the classification of open water, young ice, growing ice and melting ice. Based on the results obtained from the comparison of various parameter combinations, Sigma0, PP, OCOG_W and LEW achieved high classification accuracies (95.46% to 95.88 %) for all four classifiers and, therefore, found to be the optimal combination for discriminating between open water and different lake ice types. Additionally, Sigma0, OCOG_W and PP were determined to be the most important parameters to the classification performance in accordance with the permutation-based feature importance results. It is important to note that all four classifiers (SVM, KNN, RF and GBT) achieved comparable accuracies in both k-fold classification and spatial cross-validation tests conducted on 11 large lakes in the Northern Hemisphere. However, on the aspect of

hyperparameters sensitivity and prediction duration, RF and KNN are found to be a better fit for global lake ice mapping as they are less sensitive to their internal hyperparameters and provide faster processing speeds.

In the case of melting ice, the waveform shape is similar to that of young ice or open water waveforms. This similarity in waveform shapes introduces fuzziness into the classification algorithms which limits the approach in distinguishing melting ice from other classes. To overcome this limitation, near-surface air temperature data (such as ERA5 2-m near-surface air temperature) could be used as an additional input parameter into the ML models along with the best waveform parameters and backscatter coefficient values. Introducing 2-m air temperature into the classifiers would likely allow for discrimination between melting ice and young ice that forms at sub-zero temperatures; misclassification of surface type classes from such cases could be avoided. Based on our findings, some misclassifications occur near or on pressure ridges formed on the ice surface. This shows that altimetry signals are sensitive to the presence of deformation features such as pressure ridges. Hence, a follow-up investigation should be conducted on the assessing the capability of the altimetry signals to identify pressure ridges in addition to the classes covered in this study. Overall, the results demonstrate that waveform parameters extracted from SAR altimetry can be used to discriminate between open water and different ice types (young ice, growing ice and melting ice).

Chapter 4

General Conclusion

4.1 Summary

This thesis presented an approach to classify open water and ice types (young ice, growing ice, and melting ice) on lakes using SAR altimetry data and machine learning models. Considering the fact that there are not many lake ice classification methods out there compared to sea ice, this study addresses a research gap in finding an optimal lake ice classification algorithm which will be helpful to researchers looking for an approach to assess water-level biases introduced by the presence of the ice and also identifying times of the ice season when the estimation of lake ice thickness may be limited (thin ice at the beginning of freeze-up) or simply not possible (melting ice with the onset of break-up).

Chapter 3 presented a study evaluating the performance of the four ML algorithms in lake ice classification from SAR altimetry data. This study shows that all the waveform configurations achieved very good classification performance with overall mean accuracies ranging from 88.06% to 96.16%. However, the Sigma0+PP+OCOG_W+LEW combination is considered the best waveform parameter configuration as it scored the best k-fold (k=10) CV accuracy across all classifiers. Despite showing comparable classification performances in overall classification, the random forest and K Nearest Neighbours classifiers are found more suitable for global lake ice mapping based on the 11 lakes included in this study. This is because both classifiers are less sensitive to their internal hyperparameters and provide faster processing speeds (~2-3 minutes per track for prediction with the trained model). Also, Sigma0, OCOG_W and PP are the most important waveform parameters contributing to the lake ice and open water classification.

Overall, the results are promising and show the usefulness of waveform parameters in discriminating between open water and different ice types. In addition, all four classifiers achieved excellent spatial cross-validation accuracies ranging from 91.08% to 99.02% in all lakes with the exception of Lake Vanern (83.58-86.66%). The high spatial cv accuracies indicate that our classification approach can cope with the spatial variability in the altimetry datasets. Besides, the irregular shoreline and compact shape of Lake Vanern may be the reason behind their comparatively lower spatial cv accuracies.

4.2 Limitations and recommendations for future work

Since melting ice (or overlaying melting snow) does not display a unique waveform shape and its waveform appears similar to the waveform shape of young ice (or open water), it causes fuzziness in the classification. This was evident through some prediction results where the observations over the melting ice class were misclassified as young ice classes. It makes sense because the backscatter coefficient is the only parameter that helps to discriminate melting ice from other classes. Ice undergoing melt does not show a unique waveform shape. To reduce the fuzziness and to further optimize the model, near-surface air temperature data (such as ERA5 2-m near-surface air temperature) could be fed into the machine learning model along with the waveform parameters and backscatter coefficient values for each observation. In this way, we could provide the algorithm another parameter to distinguish melting ice from young ice that forms at sub-zero temperatures. It is very much possible to avoid such a kind of misclassification.

Based on the prediction results generated by our classification algorithms, it is clear that a few misclassifications occur near or on pressure ridges formed on the ice surface. This supports the fact that altimetry signals are sensitive to the presence of deformation features such as pressure ridges. Hence, a further study on the capability of the altimetry signals to identify pressure ridges would be helpful.

Moreover, in our study, only a three-year dataset was used, which limited us from performing temporal cross-validation and further investigating temporal changes in the lakes investigated. The timing of ice formation, decay and ice cover duration varies annually due to weather conditions. As a result, the occurrence of each surface type (open water, young ice, growing ice or melting ice) on the lake may not be the same across years; for example, on the same date, one year may be characterized by more growing ice due to cold conditions, and another year may show more young ice due to later ice formation and milder temperatures. Thus, to maintain a class balance in temporal cross-validation, more ice seasons (dataset of many years) could be added in a follow-up study, and a large sample of different classes could be collected to feed into our machine learning classifiers.

The classification algorithms developed in this thesis were designed for use with SAR backscatter and waveforms only; hence, further work is needed to assess the potential of the algorithms introduced herein to LRM waveforms. This is because LRM and SAR waveform shapes are different (not shown here), especially the trailing edge of the LRM waveforms displays

many peaks, and few of the parameters applied in this thesis to data acquired in SAR mode depend on the peak. In addition, the along-track resolution of the LRM (~2-20 km) is low compared to SAR (~300 m). However, most of the available altimetry data are from conventional altimeters (dating back to about 1991), which produce LRM waveforms. As we aim to create an optimal classification approach, our algorithm must be compatible with all the available radar altimetry datasets. Future studies will be conducted to attain this goal.

References

Adrian, R., O'Reilly, C. M., Zagarese, H., Baines, S. B., Hessen, D. O., Keller, W., et al. (2009). Lakes as sentinels of climate change. *Limnology and Oceanography*, *54*(6), 2283–2297.

Ashton, G. D. (2011). River and lake ice thickening, thinning, and snow ice formation. *Cold Regions Science and Technology*, *68*(1), 3–19. https://doi.org/10.1016/j.coldregions.2011.05.004

Aviso+ (2022). Timeline of modern radar altimetry missions. https://doi.org/10.24400/527896/A02-2022.001 version YYYY/MM"

Beckers, J. F., Alec Casey, J., & Haas, C. (2017). Retrievals of lake ice thickness from Great Slave Lake and Great Bear Lake using CryoSat-2. *IEEE Transactions on Geoscience and Remote Sensing*, *55*(7), 3708–3720. https://doi.org/10.1109/TGRS.2017.2677583

Belward, A., Bourassa, M., Dowell, M., Briggs, S., Dolman, H., Holmlund, K., et al. (2016). The Global Observing System for Climate: Implementation Needs. GCOS 200.

Buontempo, C., Dolman, H., Krug, T., Schmetz, J., Speich, S., Thorne, P., et al. (2022). The 2022 GCOS Implementation Plan. GCOS 244.

Bengtsson, L. (1986). Spatial Variability of Lake Ice Covers. *Geografiska Annaler: Series A, Physical Geography*, *68*(1–2), 113–121. https://doi.org/10.1080/04353676.1986.11880164

Benson, B., J. Magnuson, and S. Sharma. (2000). Global lake and river ice phenology database, version 1 [Data Set]. Boulder, Colorado, USA. National Snow and Ice Data Center. https://doi.org/10.7265/N5W66HP8. Date Accessed 10-31-2022.

Birkett, C. M. (1995). The contribution of TOPEX/POSEIDON to the global monitoring of climatically sensitive lakes. *Journal of Geophysical Research: Oceans*, *100*(C12), 25179–25204. https://doi.org/10.1029/95JC02125

Birkett, C. M., & Beckley, B. (2010). Investigating the performance of the Jason-2/OSTM radar altimeter over lakes and reservoirs. *Marine Geodesy*, *33*(sup1), 204–238. https://doi.org/10.1080/01490419.2010.488983

Birkett, C., Reynolds, C., Beckley, B., & Doorn, B. (2011). From research to operations: The USDA Global Reservoir and Lake Monitor. In S. Vignudelli, A. G. Kostianoy, P. Cipollini, & J. Benveniste (Eds.), *Coastal Altimetry* (pp. 19–50). Springer. https://doi.org/10.1007/978-3-642-12796-0_2

Brown, L. C., & Duguay, C. R. (2010). The response and role of ice cover in lake-climate interactions. *Progress in Physical Geography: Earth and Environment*, *34*(5), 671–704. https://doi.org/10.1177/0309133310375653

Cai, Y., Duguay, C. R., & Ke, C.-Q. (2022). A 41-year (1979–2019) passive-microwave-derived Lake Ice Phenology Data record of the Northern Hemisphere. *Earth System Science Data*, *14*(7), 3329–3347. https://doi.org/10.5194/essd-14-3329-2022

Carrea, L., Embury, O., & Merchant, C. J. (2015). *GloboLakes: High-resolution global limnology dataset v1* (1.0) [Data set]. NERC Centre for Environmental Data Analysis (CEDA). https://doi.org/10.5285/6BE871BC-9572-4345-BB9A-2C42D9D85CEB

Carrea, L., & Merchant, C. J. (2019). *GloboLakes: Lake Surface Water Temperature (LSWT) v4.0 (1995-2016)* (3.1) [Application/xml]. Centre for Environmental Data Analysis (CEDA). https://doi.org/10.5285/76A29C5B55204B66A40308FC2BA9CDB3

Crétaux, J.-F., Arsen, A., Calmant, S., Kouraev, A., Vuglinski, V., Bergé-Nguyen, M., Gennero, M.-C., Nino, F., Abarca Del Rio, R., Cazenave, A., & Maisongrande, P. (2011). SOLS: A

lake database to monitor in the Near Real Time water level and storage variations from remote sensing data. *Advances in Space Research*, *47*(9), 1497–1507. https://doi.org/10.1016/j.asr.2011.01.004

Crétaux, J.-F., & Birkett, C. (2006). Lake studies from satellite radar altimetry. *Comptes Rendus Geoscience*, *338*(14), 1098–1112. https://doi.org/10.1016/j.crte.2006.08.002

Crétaux, J.-F., Merchant, C. J., Duguay, C., Simis, S., Calmettes, B., Bergé-Nguyen, M., Wu, Y., Zhang, D., Carrea, L., Liu, X., Selmes, N., & Warren, M. (2020). *ESA Lakes Climate Change Initiative (Lakes_cci): Lake products, Version 1.0* [Application/xml]. Centre for Environmental Data Analysis (CEDA). https://doi.org/10.5285/3C324BB4EE394D0D876FE2E1DB217378

Dinardo, S., Fenoglio-Marc, L., Buchhaupt, C., Becker, M., Scharroo, R., Joana Fernandes, M., & Benveniste, J. (2018). Coastal SAR and PLRM altimetry in German Bight and West Baltic Sea. *Advances in Space Research*, *62*(6), 1371–1404. https://doi.org/10.1016/j.asr.2017.12.018

Du, J., Kimball, J. S., Duguay, C., Kim, Y., & Watts, J. D. (2017). Satellite microwave assessment of Northern Hemisphere lake ice phenology from 2002 to 2015. *The Cryosphere*, *11*(1), 47–63. https://doi.org/10.5194/tc-11-47-2017

Duguay, C. R., Bernier, M., Gauthier, Y., & Kouraev, A. (2015). Remote sensing of lake and river ice. In *Remote Sensing of the Cryosphere* (pp. 273–306).

Duguay, C. R., Flato, G. M., Jeffries, M. O., Ménard, P., Morris, K., & Rouse, W. R. (2003). Ice-cover variability on shallow lakes at high latitudes: Model simulations and observations. *Hydrological Processes*, *17*(17), 3465–3483. https://doi.org/10.1002/hyp.1394

Duguay, C. R., Pultz, T. J., Lafleur, P. M., & Drai, D. (2002). RADARSAT backscatter characteristics of ice growing on shallow sub-Arctic lakes, Churchill, Manitoba, Canada. *Hydrological Processes*, *16*(8), 1631–1644. https://doi.org/10.1002/hyp.1026

Fredensborg Hansen, R. M., Rinne, E., & Skourup, H. (2021). Classification of sea ice types in the Arctic by radar echoes from SARAL/AltiKa. *Remote Sensing*, *13*(16), Article 16. https://doi.org/10.3390/rs13163183

Fu, L.-L., & Cazenave, A. (2000). *Satellite Altimetry and Earth Sciences: A Handbook of Techniques and Applications*. Elsevier.

Gao, Q., Makhoul, E., Escorihuela, M. J., Zribi, M., Quintana Seguí, P., García, P., & Roca, M. (2019). Analysis of retrackers' performances and water level retrieval over the Ebro River Basin using Sentinel-3. *Remote Sensing*, *11*(6), Article 6. https://doi.org/10.3390/rs11060718

Heron, R., & Woo, M.-K. (1994). Decay of a High Arctic lake-ice cover: Observations and modelling. *Journal of Glaciology*, *40*(135), 283–292. https://doi.org/10.3189/S0022143000007371

Jeffries, M., Morris, K., & Duguay, C. (2012). *Floating ice: Lake ice and river ice* (pp. A381–A424).

Jeffries, M. O., Morris, K., & Kozlenko, N. (2005). Ice characteristics and processes, and remote sensing of frozen rivers and lakes. In *Remote Sensing in Northern Hydrology: Measuring Environmental Change* (pp. 63–90). American Geophysical Union (AGU). https://doi.org/10.1029/163GM05

Kang, K.-K., Duguay, C. R., & Howell, S. E. L. (2012). Estimating ice phenology on large northern lakes from AMSR-E: Algorithm development and application to Great Bear Lake and

Great Slave Lake, Canada. *The Cryosphere*, *6*(2), 235–254. https://doi.org/10.5194/tc-6-235-2012

Kouraev, A. V., Papa, F., Buharizin, P. I., Cazenave, A., Crétaux, J. F., Dozortseva, J., & Remy, F. (2003). Ice cover variability in the Caspian and Aral seas from active and passive microwave satellite data. *Polar Research, 22(1),* 43-50.

Kouraev, A. V., Semovski, S. V., Shimaraev, M. N., Mognard, N. M., Legrésy, B., & Remy, F. (2007). Observations of Lake Baikal ice from satellite altimetry and radiometry. *Remote Sensing of Environment, 108*(3), 240–253. https://doi.org/10.1016/j.rse.2006.11.010

Kouraev, A. V., Shimaraev, M. N., Buharizin, P. I., Naumenko, M. A., Crétaux, J.-F., Mognard, N., Legrésy, B., & Rémy, F. (2008). Ice and snow cover of continental water bodies from simultaneous radar altimetry and radiometry observations. *Surveys in Geophysics*, *29*(4), 271–295. https://doi.org/10.1007/s10712-008-9042-2

Liibusk, A., Kall, T., Rikka, S., Uiboupin, R., Suursaar, Ü., & Tseng, K.-H. (2020). Validation of Copernicus sea level altimetry products in the Baltic Sea and Estonian lakes. *Remote Sensing, 12(24), 4062. MDPI AG*. Retrieved from http://dx.doi.org/10.3390/rs12244062

Mangilli, A., Thibaut, P., Duguay, C. R., & Murfitt, J. (2022). A new approach for the estimation of lake ice thickness from conventional radar altimetry. *IEEE Transactions on Geoscience and Remote Sensing*, *60*, 1–15. https://doi.org/10.1109/tgrs.2022.3186253

Messager, M.L., Lehner, B., Grill, G., Nedeva, I., Schmitt, O. (2016). Estimating the volume and age of water stored in global lakes using a geo-statistical approach. *Nature Communications, 7: 13603.* https://doi.org/10.1038/ncomms13603

Müller, F. L., Dettmering, D., Bosch, W., & Seitz, F. (2017). Monitoring the Arctic Seas: How satellite altimetry can be used to detect open water in sea-ice regions. *Remote Sensing*, *9*(6), Article 6. https://doi.org/10.3390/rs9060551

Murfitt, J., & Duguay, C. R. (2021). 50 years of lake ice research from active microwave remote

sensing: Progress and prospects. *Remote Sensing of Environment*, *264*, 112616.

Nielsen, K., Andersen, O. B., & Ranndal, H. (2020). Validation of Sentinel-3A based lake level over US and Canada. *Remote Sensing*, *12*(17), Article 17. https://doi.org/10.3390/rs12172835

Nilsson, J., Vallelonga, P., Simonsen, S. B., Sørensen, L. S., Forsberg, R., Dahl-Jensen, D., Hirabayashi, M., Goto-Azuma, K., Hvidberg, C. S., Kjær, H. A., & Satow, K. (2015). Greenland 2012 melt event effects on CryoSat-2 radar altimetry. *Geophysical Research Letters*, *42*(10), 3919–3926. https://doi.org/10.1002/2015GL063296

NSIDC-National Snow and Ice Data Center (comp.). (1995). Great Lakes Surface Ice Reports from U.S. Coast Guard, 1961 - 2004, Version 1 [Data Set]. Boulder, Colorado USA. National Snow and Ice Data Center. https://doi.org/10.7265/N5BG2KW2. Date Accessed 10-29-2022.

NSIDC-National Snow & Ice Data Center, . (2004). Great Lakes Ice Charts, Version 1 [Data Set]. Boulder, Colorado USA. National Snow and Ice Data Center. https://doi.org/10.7265/N5H41PBV. Date Accessed 10-29-2022.

PODAAC (2022). Altimetric Data Information: Missions| PO. DAAC/ JPL/ NASA. Physical Oceanography Distributed Active Archive Center (PO.DAAC), accessed 23 October 2022, https://podaac.jpl.nasa.gov/Altimetric_Data_Information/Missions.

Raney, R. K. (1998). The delay/Doppler radar altimeter. *IEEE Transactions on Geoscience and Remote Sensing*, *36*(5), 1578–1588. https://doi.org/10.1109/36.718861

Ricker, R., Hendricks, S., Helm, V., Skourup, H., & Davidson, M. (2014). Sensitivity of CryoSat-2 Arctic sea-ice freeboard and thickness on radar-waveform interpretation. *The Cryosphere*, *8*(4), 1607–1622. https://doi.org/10.5194/tc-8-1607-2014

Ricko, M., Carton, J. A., Birkett, C. M., & Cretaux, J.-F. (2012). Intercomparison and validation of continental water level products derived from satellite radar altimetry. *Journal of Applied Remote Sensing*, *6*(1), 061710. https://doi.org/10.1117/1.JRS.6.061710

Rinne, E., & Similä, M. (2016). Utilisation of CryoSat-2 SAR altimeter in operational ice charting. *The Cryosphere*, *10*(1), 121–131. https://doi.org/10.5194/tc-10-121-2016

Rosenzweig, C., Casassa, G., Karoly, D., Imeson, A., Liu, C., Menzel, A., Rawlins, S., Root, T., Seguin, B., & Tryjanowski, P. (2007). *Assessment of observed changes and responses in natural and managed systems*. https://doi.org/10.5167/uzh-33180

Sarmiento, S. E., & Khan, S. D. (2010). Spatial–temporal variability of Great Slave Lake levels from satellite altimetry. *IEEE Geoscience and Remote Sensing Letters*, *7*(3), 426–429. https://doi.org/10.1109/LGRS.2009.2038178

Schwatke, C., Dettmering, D., Bosch, W., & Seitz, F. (2015). DAHITI – an innovative approach for estimating water level time series over inland waters using multi-mission satellite altimetry. *Hydrology and Earth System Sciences*, *19*(10), 4345–4364. https://doi.org/10.5194/hess-19-4345-2015

Sentinel-3 User Guides (2022). Sentinel Online, accessed 23 October 23, 2022, https://sentinels.copernicus.eu/web/sentinel/user-guides/sentinel-3-altimetry

Sharma, S., Gray, D. K., Read, J. S., O'Reilly, C. M., Schneider, P., Qudrat, A., Gries, C., Stefanoff, S., Hampton, S. E., Hook, S., Lenters, J. D., Livingstone, D. M., McIntyre, P. B., Adrian, R., Allan, M. G., Anneville, O., Arvola, L., Austin, J., Bailey, J., … Woo, K. H. (2015). A global database of lake surface temperatures collected by in situ and satellite methods from 1985–2009. *Scientific Data*, *2*(1), Article 1. https://doi.org/10.1038/sdata.2015.8

Sharma, S., Richardson, D., Woolway, R., Imrit, M., Bouffard, D., Blagrave, K., Daly, J., Filazzola, A., Granin, N., Korhonen, J., Magnuson, J., Marszelewski, W., Matsuzaki, S., Perry, W., Robertson, D., Rudstam, L., Weyhenmeyer, G., & Yao, H. (2021). Loss of ice cover, shifting phenology, and more extreme events in Northern Hemisphere lakes. *Journal of Geophysical Research: Biogeosciences*, *126*. https://doi.org/10.1029/2021JG006348

Shen, X., Zhang, J., Meng, J., Zhang, J., & Ke, C. (2017a). Sea ice type classification based on random forest machine learning with Cryosat-2 altimeter data. *2017 International Workshop on Remote Sensing with Intelligent Processing (RSIP)*, 1–5. https://doi.org/10.1109/RSIP.2017.7958792

Shen, X., Zhang, J., Zhang, X., Meng, J., & Ke, C. (2017b). Sea ice classification using Cryosat-2 altimeter data by optimal classifier–feature assembly. *IEEE Geoscience and Remote Sensing Letters*, *14*(11), 1948–1952. https://doi.org/10.1109/LGRS.2017.2743339

Shu, S., Liu, H., Beck, R. A., Frappart, F., Korhonen, J., Xu, M., Yang, B., Hinkel, K. M., Huang, Y., & Yu, B. (2020a). Analysis of Sentinel-3 SAR altimetry waveform retracking algorithms for deriving temporally consistent water levels over ice-covered lakes. *Remote Sensing of Environment*, *239*, 111643. https://doi.org/10.1016/j.rse.2020.111643

Shu, S., Zhou, X., Shen, X., Liu, Z., Tang, Q., Li, H., Ke, C., & Li, J. (2020b). Discrimination of different sea ice types from CryoSat-2 satellite data using an Object-based Random Forest (ORF). *Marine Geodesy*, *43*(3), 213–233. https://doi.org/10.1080/01490419.2019.1671560

Sleator, F. E. (1995). GLERL Great Lakes Ice Thickness Data Base, 1966-1979, Version 1 [Data Set]. Boulder, Colorado USA. National Snow and Ice Data Center. https://doi.org/10.7265/N5KW5CXG. Date Accessed 10-29-2022.

Tilling, R. L., Ridout, A., & Shepherd, A. (2018). Estimating Arctic sea ice thickness and volume using CryoSat-2 radar altimeter data. *Advances in Space Research*, *62*(6), 1203–1225. https://doi.org/10.1016/j.asr.2017.10.051

Tilling, R., Kurtz, N. T., Bagnardi, M., Petty, A. A., & Kwok, R. (2020). Detection of melt ponds on Arctic Summer Sea ice from icesat-2. *Geophysical Research Letters*, *47(23).* https://doi.org/10.1029/2020gl090644

Tournadre, J., & Chaprono, B. (2020). Altimeter as an imager of the sea surface roughness: Comparison of SAR and LRM modes. *IGARSS 2020 - 2020 IEEE International Geoscience and Remote Sensing Symposium.* https://doi.org/10.1109/igarss39084.2020.9323226

Wernecke, A., & Kaleschke, L. (2015). Lead detection in Arctic sea ice from CryoSat-2: Quality assessment, lead area fraction and width distribution. *The Cryosphere*, *9*(5), 1955–1968. https://doi.org/10.5194/tc-9-1955-2015

Wiese, M., Griewank, P., & Notz, D. (2015). On the thermodynamics of melting sea ice versus melting freshwater ice. *Annals of Glaciology, 56(69), 191-199.* doi:10.3189/2015AoG69A874

Williams, G. P. (1965). Correlating freeze-up and break-up with weather conditions. *Canadian Geotechnical Journal*, *2*(4), 313–326. https://doi.org/10.1139/t65-047

Wu, Y., Duguay, C. R., & Xu, L. (2021). Assessment of machine learning classifiers for global lake ice cover mapping from MODIS TOA reflectance data. *Remote Sensing of Environment*, *253*, 112206. https://doi.org/10.1016/j.rse.2020.112206

Zakharova, E. A., Fleury, S., Guerreiro, K., Willmes, S., Rémy, F., Kouraev, A. V., & Heinemann, G. (2015). Sea ice leads detection using SARAL/AltiKa altimeter. *Marine Geodesy*, *38*(sup1), 522–533. https://doi.org/10.1080/01490419.2015.1019655

Ziyad, J., Goïta, K., Magagi, R., Blarel, F., & Frappart, F. (2020). Improving the estimation of water level over freshwater ice cover using altimetry satellite active and passive observations. *Remote Sensing*, *12*(6), Article 6. https://doi.org/10.3390/rs12060967

Zygmuntowska, M., Khvorostovsky, K., Helm, V., & Sandven, S. (2013). Waveform classification of airborne synthetic aperture radar altimeter over Arctic sea ice. *The Cryosphere*, *7*(4), 1315–1324. https://doi.org/10.5194/tc-7-1315-2013